TWO-DIMENSIONAL SELECTIVELY THINNED STEEL MICROMIRRORS

by

Betül KÜÇÜKAKARSU USTA

B.S., Electrical and Electronics Engineering, Bogazici University, 2009

Submitted to the Institute for Graduate Studies in
Science and Engineering in partial fulfillment of
the requirements for the degree of
Master of Science

Graduate Program in Electrical and Electronics Engineering
Boğaziçi University

2011

ACKNOWLEDGEMENTS

I would like to express my profound sense of gratitude to my thesis supervisor Prof. Arda D. Yalçınkaya for his guidance and inspirational teaching throughout this endeavour. His solid theoretical background and experience in the field have opened and smoothed the way to my research. I wish to acknowledge my indebtedness to Prof. Şenol Mutlu for his bright ideas, constant support, and invaluable efforts at many stages in the course of this research. I would like to sincerely thank Prof. Çetin Yılmaz for sharing his knowledge and taking part in my thesis jury. I would like to thank Prof. Günhan Dündar for his guidance especially in the beginning of my master's study. I would like to express my special thanks to Dağhan Gökdel, PhD for his kind support, guidance, and generosity in sharing his knowledge and experience. I would like to also thank Baykal Sarıoğlu for helping me overcome many obstacles during my research studies. It is my pleasure to thank my colleagues in MNL, BUMEMS, and Beta Lab, especially Engin Afacan, Umut Çindemir, Gürkan Sönmez, İskender Haydaroğlu, Okan Z. Batur, Işıl Kalafat Kızılkaya, Melih Akçakaya, and Orhan Mert, for their support, friendship, and inspiring ideas. I am thankful to Mehmet Ali Yorulmaz and Eksper Wire Cut and Mold Facility for their convenience and expertise in machining the scanners.

I owe my deepest gratitude to my beloved parents, Ayla and Namık Küçükakarsu, who have had the greatest influence by providing a fostering environment full of care, advice, and sacrifice for me to grow in. I would like to sincerely thank my grandparents for not sparing any efforts since I was born. I would like to also thank my parents-in-law, Emine and Mehmet Usta, for supporting me and my husband in being a family and encouraging to lead our academic studies. I would like to thank many friends, in particular Havva Karamanlı, Başak Öztaş Yoldemir, Simge Ay, and Ayça Işıksal, for their support throughout these two years.

Last but not the least, I owe my sincere gratitude to my husband, Mehmet Usta, for his continuous support, compassion, and invaluable company.

ABSTRACT

TWO-DIMENSIONAL SELECTIVELY THINNED STEEL MICROMIRRORS

This thesis mainly deals with electromagnetically actuated resonant steel MOEMS scanners developed for a scanner-based projection system and focuses on the design of micromirrors to achieve QVGA and VGA specs. Types of scanners designed for this work are 2D gimballed torsional scanner and its design variations with the addition of sub-arms and increasing the number of beams in inner and/or outer frames. Stainless steel 420 is used as the structural material. Selective thinning is applied in the fabrication of some designs. Resonant-mode dynamic actuation is done with a time-varying current carrying external coil. Two different techniques are used for the fabrication of scanners: (i) electrochemical etching after photolithographic process (ii) electric discharge machining (EDM). In order to increase the total optical scan angle (TOSA), designs favoring the mechanical coupling are employed.

ÖZET

SEÇİCİ OLARAK İNCELTİLMİŞ İKİ BOYUTLU ÇELİK MİKRO AYNALAR

Bu tez, esas olarak, tarama tabanlı projeksiyon sisteminde kullanılmak üzere, elektromanyetik olarak eylenen çelik mikro-opto-elektro-mekanik aynalar üzerinedir; QVGA ve VGA ekran yeterliliklerine sahip mikroaynaların tasarımına odaklanmıştır. Bu çalışma için tasarlanmış tarayıcı çeşitleri iki boyutlu askılı bağlanmış burunumsal tarayıcı ve bu tasarımın tali kol eklenmiş, iç ve/veya dış kiriş sayıları artırılmış varyasyonlarıdır. Bazı tasarımların iç ayna ve dış kirişlerinde inceltme işlemi uygulanmıştır. Yapısal malzeme olarak paslanmaz çelik SS 420 maddesi kullanılmıştır. Eyleme işlemi alternatif akım taşıyan bir bobin vasıtasıyla yapılmıştır. Aynaların üretiminde iki farklı yöntem kullanılmıştır: (i) fotolitografi sonrası elektrokimyasal aşındırma (ii) elektro-erozyon (EDM). Toplam optik tarama açısını yükseltmek için mekanik kuplajı artıracak tasarımlar kullanılmiıştır.

TABLE OF CONTENTS

LIST OF FIGURES

LIST OF TABLES

LIST OF SYMBOLS

a	Aperture shape factor
B	Magnetic field density
$(BH)_{max}$	Energy product
C_ϕ	Angular damping coefficient
E	Young's modulus
D	Beam diameter
dl	Elemental length
F	Force
f_h	Horizontal scan frequency
f_{res}	Resonance frequency
f_v	Vertical scan frequency
G	Torsional modulus
H	Magnetic field
H_c	Coercive field
H_2SO_4	Sulphuric acid
H_3PO_4	Phosphoric acid
HCl	Hydrogen chloride
I	Current
I_{xx}	Second moment of area about x-axis
I_{yy}	Second moment of area about y-axis
I_{zz}	Second moment of area about z-axis
$J_{f,xx}$	Mass moment of inertia due to flexures
J_m	Effective mass moment of inertia
J_z	Polar moment of inertia about z-axis
k	Spring constant
k_ϕ	Angular spring constant
K	Torsional stiffness
K_{anis}	Magnetic anisotropy constant
K_f	Flexural stiffness

K_s	Torsional spring constant
K_{sys}	Coefficient for the effects of system design parameters
K_T	Beam truncation coefficient
L_f	Flexural length
m	Mass
$\vec{m}$	Magnetic moment
M	Magnetization
M_f	Flexural mass
M_m	Mirror mass
M_r	Remanent magnetization
M_s	Saturation magnetization
N	Number of resolvable spots
N_h	Horizontal resolution
N_h	Vertical resolution
$NaCl$	Sodium chloride
Q	Total charge
$Q - factor$	Quality factor
S	Pole surface
t_m	Mirror thickness
T	Beam truncation ratio
$\vec{T}$	Torque
$\vec{T}_{anis}$	Anisotropy torque
$\vec{T}_{field}$	Field torque
$\vec{T}_{mech}$	Mechanical restoring torque
U_{ms}	Magnetostatic energy
V	Volume of the material under magnetization
ZnO	Zinc oxide
$\delta\theta$	Beam divergence
η_m	Magnetic charge density
θ	Angle of rotation

θD	Product of mechanical scan angle and mirror diameter
θ_{max}	Maximum optical scan angle
θ_{mech}	Mechanical scan angle
θ_{opt}	Optical scan angle
λ	Wavelength of the incident light
λ	Line current density
ν	Poisson's ratio
$\vec{\nu}$	Velocity of charge
μ_0	Permeability of free space
μ_r	Relative magnetic permeability
ρ	Material density
σ_y	Yield stress
φ	Total magnetic charge
χ	Susceptibility
ω	Angular frequency

LIST OF ACRONYMS/ABBREVIATIONS

1D	One Dimensional
2D	Two Dimensional
AC	Alternating Current
CRT	Cathode Ray Tube
DC	Direct Current
DI	Deionized
EDM	Electric Discharge Machining
HDTV	High-definition Television
IPA	Isopropyl Alcohol
LCD	Liquid Crystal Display
MEMS	Microelectromechanical Systems
MOEMS	Micro-opto-electromechanical Systems
PC	Personal Computer
PR	Photoresist
PZT	Lead Zirconate Titanate
QVGA	Quarter Video Graphics Array
SS	Stainless Steel
SVGA	Super Video Graphics Array
SXGA	Super Extended Video Graphics Array
TOSA	Total Optical Scan Angle
UV	Ultra Violet
UXGA	Ultra Extended Video Graphics Array
VGA	Video Graphics Array
XGA	Extended Graphics Array

1. INTRODUCTION

An optical scanner is a device used for directing a beam of light in specified directions. An optical scanning system contains a light source, a mirror, a beamsplitter, and a detector. The light source is commonly a commercial laser diode with polarizer and lens. In macro scale, oscillatory and galvanometric systems are present. MEMS based micromirrors can replace macromirrors where there is need for miniaturization, light weight, increased reliability, reduced cost, and low energy consumption. Most optical scanners use movable mirrors. Figure 1.1 shows the operation principle for a tilting-mirror. By using the resonant vibration of a tilting-mirror, an optical scan angle proportional to mirror deflection can be achieved. Besides deflection, refraction and diffraction based optical scanners are present.

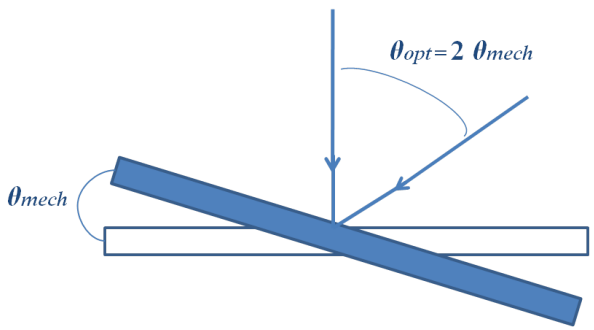

Figure 1.1. Scan angle of a tilting-mirror.

General performance criteria for a scanning micromirror are maximum scan angle, resolution, resonant frequency, device size, surface flatness, power consumption (actuation voltage and/or current), compatibility with integated electronic circuitry, and structural stability.

For raster-scanning applications a dual-axis system is required. This can be the combination of two 1D scanners or a single biaxial scanner as shown in Figure 1.2 [8].

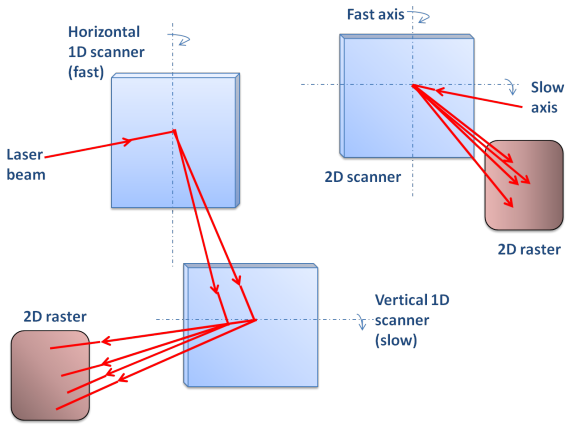

Figure 1.2. Raster scanning setup with cascaded 1-D scanners and a single 2-D scanner.

1.1. MEMS Micromirror Based Display Systems

Two dominant display technologies, the cathode ray tube (CRT) and the liquid crystal display (LCD) have been on the market since 1930s and late 1960s, respectively. Using MEMS technology in display systems is a relatively new concept. The 'mirror matrix tube' developed at Westinghouse Research Labs in mid-1970s was the earliest micromechanical projection display device [9]. Micromechanical light modulators were developed by IBM for display applications [10]. A projection display using a 16×1 array of single-crystal cantilever micromechanical light modulators and a galvanometric scanner and silicon torsional mirrors were demonstrated by K. E. Petersen [11]. A more recent example of MEMS mirror application in display technology is the 'normal augmented vision system' (NOMAD) which is a wearable personal display product developed by Microvision [12]. Texas Instruments Digital Micromirror Device (DMD) display is an array of square micromirrors, each corresponding to a single pixel in the projected image.

Mirror producing angular motion is used to deflect a modulated light beam on an image plane to create a display. A micromirror can be used to change the direction of propagation of a light beam thereby scanning or modulating the beam. Scanned light beam is a patented method for optical imaging [13]. Micromechanical light modulators such as diffraction gratings, optical choppers, or microinterferometers are parts of the micro-opto-electro-mechanical systems, abbreviated as MOEMS. MOEMS display and

imaging have found applications such as wearable displays, projection displays, barcode readers, and infrared imaging cameras in industrial, medical, consumer, aerospace, and defense markets [3].

1.1.1. Laser Scanners

Laser scanning systems are advantegous in terms of resolution since one scanner can be used in scanning the multiple beams at the same time. Table 1.1 lists some of the applications of laser scanning technology.

Table 1.1. Applications of Laser Scanning Technology. After [6].

Inputs	**Outputs**
Image Digitizing	Image Recording/Printing
Bar Code Reading	Color Image Reproduction
Optical Inspection	Medical Imaging
PC Board Inspection	Data Marking and Engraving
Optical Character Recognition	Microimage Recording
Optical Data Read-Out	Reconnaissance Recording
Graphic Arts Process Camera	Optical Data Storage
Scanning Microscopy	Phototypesetting
Color Separation	Graphic Arts Platemaking
Robot Vision	Electronic Mail
Laser Radar	Earth Resources Imaging
Mensuration	Data/Image Display
Scientific Analysis	Scientific Imaging

1.1.2. Performance Criteria for Projection Systems

In raster-mode scanning, screen is scanned line-by-line with synchronous control of the actuation signal of both orthogonal axes. Figure 1.3 shows the operating principle of a projection display.

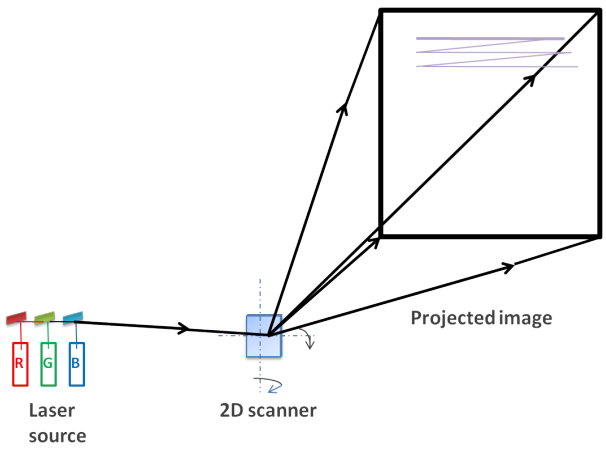

Figure 1.3. Operating principle of a projection display.

Scan angle required to move the tip of the mirror by $\lambda/2$ determines the highest resolvable spatial frequency and motion of the tip of the mirror is proportional to the product of scan angle and mirror diameter, θD product. The number of resolvable spots is called the resolution and has the formula

$$N = \frac{\theta_{max}}{\delta\theta} = \frac{\theta_{max} D}{a\lambda} \tag{1.1}$$

where θ_{max} is total optical scan range, $\delta\theta$ is beam divergence, D is the mirror diameter, a is the aperture shape factor which is 1 for square aperture, 1.22 for circular and λ is the wavelength of the incident light.

In scanning displays θD product and horizontal (f_h) determines the resolution, and vertical (f_v) scan frequencies determine the refresh rate. Table 1.2 lists the requirements for various display formats.

Table 1.2. θD product and scanner frequency requirements for various display formats. After [7].

Display Format	**QVGA**	**VGA**	**SVGA**	**XGA**	**SXGA**	**UXGA**	**HDTV**
Horizontal Resolution - N_h	320	640	800	1024	1280	1600	1920
Vertical Resolution - N_v	240	480	600	768	1024	1200	1080
$\theta \cdot D(deg \cdot mm)$	3.9	7.8	9.7	12.4	15.6	19.4	23.3
Horizontal Scanner Frequency - $f_h(kHz)$	8	16	20	25.6	34.133	40	36

For systems using diffraction-limited laser beam as the illumination source, resolution is given by [1, 7]

$$N = \frac{K_{sys}\theta_{opt}D}{K_T\lambda} = \frac{4K_{sys}\theta_{mech}D}{K_T\lambda} \tag{1.2}$$

where K_{sys} is a coefficient for the effects of system design parameters such as spot size to pixel size ratio, overscan, and type of the scanning (unidirectional or bidirectional), θ_{opt} is the full optical scan angle, θ_{mech} is the mechanical zero-to-peak angle, and K_T is a constant which is a function of beam truncation ratio, T. Typically K_{sys} is in the order of unity (about 2 for bidirectional scanning) and K_T is between 1.04 and 1.5.

Figure 1.4 illustrates the 2-D raster for unidirectional and bidirectional scanning. In bidirectional scanning, the beam reflected from the mirror scans symmetrically in both directions whereas in unidirectional scanning the laser beam returns to start position of the new line rapidly at the end of each line scan. Required horizontal scan frequency is halved for bidirectional scanning. Time-domain scanner control signals are given in Figure 1.5.

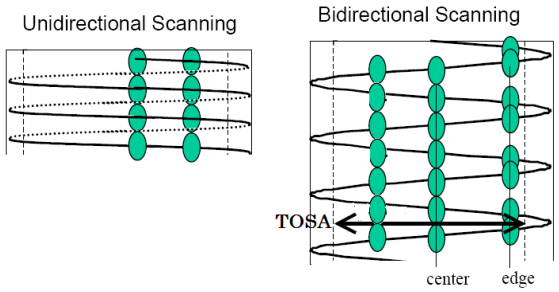

Figure 1.4. 2-D raster for unidirectional and bidirectional scanning. After [1].

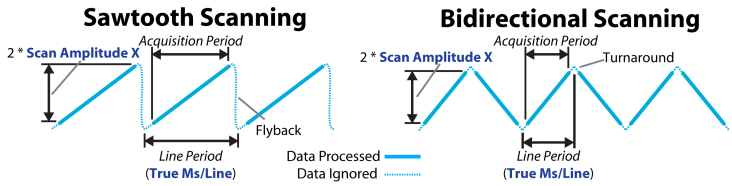

Figure 1.5. Time-domain scanner control signals for sawtooh and bidirectional scanning. After [2].

1.2. Actuation Methods for Micromirrors

In order to have mechanical motion in a microsystem a mechanism that converts some other form of energy into mechanical energy must be used. These energy conversion mechanisms are called actuation. Different types of actuation, each using different physical principles, are employed in integrated microsystems. Most widely used ones include electrostatic, thermal, piezoelectric, and electromagnetic actuations. Table 1.3 provides several performance parameters for these actuation techniques [3].

Some explanations are given to interprete the parameters given in Table 1.3 and state basic advantages and disadvantages of the main actuation schemes:

- *Electrostatic* actuation requires high actuation voltage; however, consumes less standing power. It has the advantage of ease in integration with electronic circuitry. Parallel-plate [14–16], comb-drive [17, 18] and force-array [19] type electrostatic ac-

tuators are present in the literature.

- *Thermal* actuation consumes larger power, has a slower response time, and is sensitive to thermal noise. However, larger rotation angles can be obtained with thermal actuators. Bimorph structure, which is the combination of two materials with different thermal expansion coefficients, is employed. Change in temperature results in bending of the bimorph structure. Several MEMS scanners employing thermal actuation are reported [20, 21].
- *Piezoelectric* actuation requires less actuation voltage and current; hence consumes less power. It provides lower displacements although obtained precision is higher. Piezoelectric crystals show a change in their acquired charge when they experience change in shape and become transducers between mechanical and electrical domains. There are examples of piezoelectric microscanners [22, 23].
- *Magnetic* actuation offers larger forces and larger displacements over longer distances. Required voltage is low whereas current is high. Although external components like electrocoil and/or permanent magnet are needed, integration with electronic circuitry is easier. Magnetic actuation can provide both attractive and repulsive forces. Moving-coil [24–26], moving-magnet [27, 28], and permalloy actuators [29–31] are common types. In electromagnetic actuation, a current-carrying conductor is placed in a magnetic field and resulting Lorentz force is used to obtain a torsional deflection. Permanent magnets are employed to build a DC magnetization. For mirrors with diameter greater than 2mm, electromagnetic actuation is advantageous since torque produced by Lorentz force is proportional to magnetic volume.

1.3. Main Contributions and Outline

This thesis mainly deals with electromagnetically actuated resonant steel MOEMS microscanners developed for a scanner-based projection system. This thesis focuses on the design of micromirrors to achieve QVGA and VGA specs. Main contributions of this thesis are listed below.

- Two-dimensional ferromagnetic scanners of different geometries are fabricated using

Table 1.3. Comparison of main MEMS actuation methods.

Actuator Type	**Displacement**(μm)	**Output Force** (μN)	**Actuation Voltage (V)**	**Frequency (Hz)**	**Work Output per Unit Volume** (J/m^3)	**Types**
Electrostatic	$0.1 - 30$	$0.1 - 10^3$	$\approx 50 - 120$	3×10^3	$10^2 - 10^5$	Parallel plate, comb drive, force array
Thermal	$10 - 100$	$10 - 10^3$	$\prec 20$	$10^2 - 10^3$	10^5	Bi-morph, pseudo-bimorph, bent-beam
Piezoelectric	≈ 10	$10 - 10^6$	$20 - 10^3$	10^4	$10^2 - 10^5$	PZT-based, ZnO-based
Magnetic	$\preceq 10^3$	$\preceq 10^5$	$10 - 100mA$ current	$10^2 - 10^4$	$10^3 - 10^5$	Magnetostatic, electromagnetic, magnetostrictive

two different methods which are both cheap and fast: (i) a single mask photolithography followed by electrochemical etching, (ii) a conventional metal shaping process like EDM.

- Selective thinning at the desired parts from 300 μm to approximately 150 μm to enhance the scanner mechanical actuation and frequency response performance is achieved.
- Steel - with its higher Young's modulus (E), higher shear modulus (G), comparable flexural mode frequency coefficient ($\sqrt{E/\rho}$), and a comparable torsion mode frequency coefficient ($\sqrt{G/\rho}$) - is proposed as an alternative structural material to traditionally used silicon for 2D microscanners for display applications achieving QVGA and VGA specs.
- SS 420 offers the advantage of inherent magnetization removing the need for any deposition which leads to stress in the structure.
- A slow scan TOSA of 78^o is achieved with 2D gimballed micromirrors. Designs favoring the mechanical coupling and high frequency actuation techniques are used to increase the fast scan displacement. A fast scan TOSA of 8^o is achieved with one of these designs.
- Electromagnetic actuation is used at frequencies up to 30 kHz. Different cores and current amplifiers are tried to improve the frequency response of the coil.
- The work in this thesis resulted in one conference article [32].

The thesis is organized such that structural properties, namely material properties and design geometries, of the scanners are given in detail in Chapter 2. Chapter 3 gives the basic mechanical foundations for the used behaviors of the structures. Used actuation scheme is discussed in Chapter 4. Methods used to fabricate the designed micromirrors are explained in Chapter 5. Conducted experiments and their results constitute Chapter 6. The final chapter states the conclusions and suggests the future work.

2. STRUCTURAL PROPERTIES OF THE SCANNERS

In order to maximize the optical scan angle, mechanical displacement of the mirror must be maximized. Natural resonant modes are utilized for this purpose since a mechanical system absorbs more energy when the frequency of its oscillations matches the system's natural frequency of vibration or its 'resonance frequency'. At resonance the response of the mirror is multiplied by the quality factor (Q) which is the ratio of a resonator's 3-dB bandwidth to its center frequency. In a system with high Q-factor the energy loss relative to the stored energy is lower.

Resonance frequency of a mechanical structure consisting of a weight suspended by a spring is given by the formula

$$f_{res} = \frac{1}{2\pi}\sqrt{\frac{k}{m}} \tag{2.1}$$

where k is the spring constant and m is the mass. As it can be inferred from Equation 2.1 material properties and structural geometry are the two eminent players in the design of the devices.

2.1. Material Choice

Two different types of steel was investigated as the structural material to the proposed scanners: SS 301 and SS 420. Steel, with its higher Young's modulus (E), higher shear modulus (G), comparable flexural mode frequency coefficient which is defined as $\sqrt{E/\rho}$, and a comparable torsion mode frequency coefficient ($\sqrt{G/\rho}$), becomes an alternative structural material to traditionally used silicon. Additionally, SS 420's inherent magnetization eliminates the need for any deposition which leads to stress in the structure. As a result, comparable mechanical quality factors, TOSA, and resonance mode frequencies can be accomplished with steel [33]. Table 2.1 compares the material properties of SS 301, SS 420 and single crystalline silicon.

Table 2.1. Material Property Coefficients for Silicon, SS 301, and SS420.

Material Property	**Symbol**	**Silicon**	**SS301**	**SS420**
Young's Modulus	$E(GPa)$	170	200	216
Shear Modulus	$G(GPa)$	51	86	80.7
Density	$\rho(kg/m^3)$	2330	8000	7700
Yield Stress	$\sigma_y(MPa)$	690	207	345
Torsion Frequency Coefficient	$\sqrt{(G/\rho)}$	4678	3278	3237
Other Mode Frequency Coefficient	$\sqrt{(E/\rho)}$	8541	5000	5296
Deformation Coefficient	ρ/E	1.37e-8	4e-8	3.56e-8
Flexure Stress Coefficient	σ_y/G	1.35e-2	2.4e-3	4.275e-3
Relative Magnetic Permeability	$\mu_r(H/m)$	1	1.02	magnetic

SS 420 is a martensitic steel that provides corrosion resistance and is magnetic in both annealed and hardened conditions. Table 2.1 shows the typical material composition for SS 420 [34].

Table 2.2. SS 420 Material Composition.

	%
Carbon	0.15 min.
Manganese	1.00 max.
Phosphorus	0.040 max.
Sulfur	0.030 max.
Silicon	1.00 max.
Chromium	12.00 - 14.00

Another advantage of using stainless steel as the structural material is in the ease of fabrication. Electrochemical etching with HCl or NaCl solutions after a single-mask photolithographic process can be used and by self-terminating etching process reported in

[5] selective thinning of the scanner is achieved. Besides, since it is electrically conductive, conventional methods such as electrical discharge machining give good results in shaping and thinning.

2.2. Geometry

Two different main geometries are used in this thesis work: gimballed torsional 2D scanner geometry shown in Figure 2.1 and 2D scanner geometries with subarms and pair of beams shown in Figure 2.2, 2.3, 2.4, and 2.5.

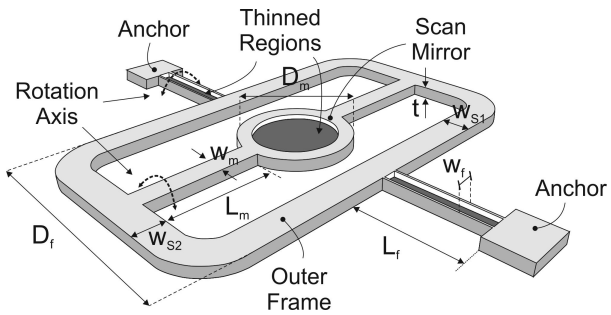

Figure 2.1. Gimballed torsional 2-D scanner geometry.

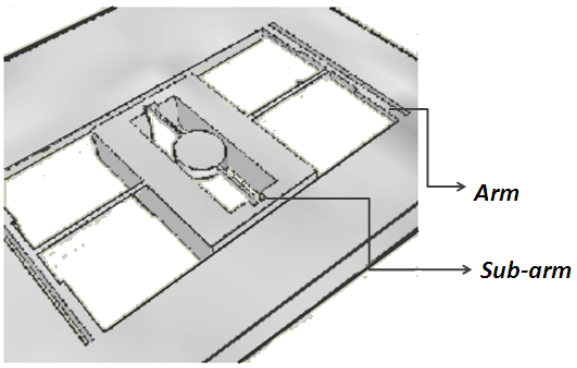

Figure 2.2. Design with sub-arms.

In these two-axis designs, the inner mirror generates the horizontal scan by rotating about the fast-scan axis while the movable frame with outer flexures form the vertical

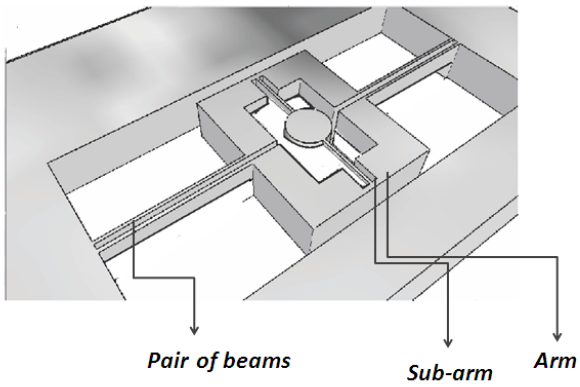

Figure 2.3. Design with sub-arms and a pair of outer flexures.

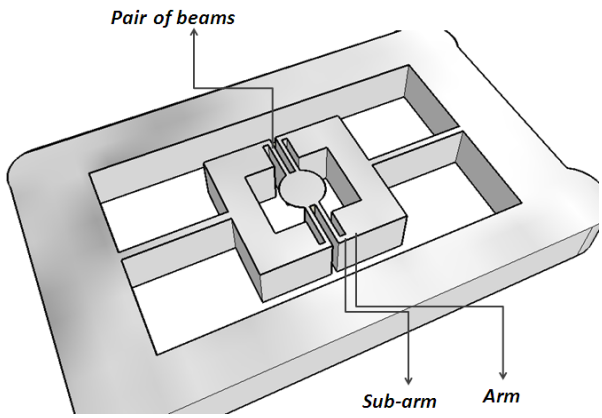

Figure 2.4. Design with sub-arms a pair of inner flexures.

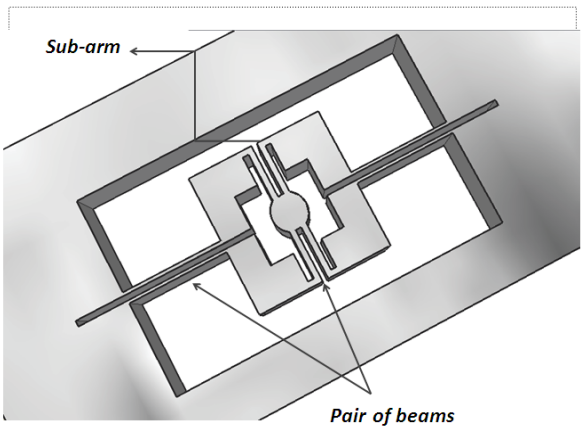

Figure 2.5. Design with sub-arms and pair of outer and inner flexures.

scan by rotating about the slow-scan axis. The slow and the fast scan modes are excited by superimposing AC signal components at the center frequencies of the corresponding resonance peaks. Hence, resonance frequency of inner mirror's torsion gives the fast-scan frequency whereas that of outer frame gives the slow-scan frequency. The ratio between these two frequencies is designed to be high since it directly affects the resolution of the scanner-based display system. Selective thinning of the outer flexures and inner mirror is employed for this purpose. According to Equation 2.1, by decreasing the mass in the mirror fast-scan frequency is increased while by decreasing the stiffness of outer flexures slow-scan frequency is lowered.

The geometry with sub-arms between torsional beams and arms is a design favoring the mechanical coupling between inner mirror and outer frame, thereby increasing the deflection [35]. This design also provides shrinking in the device size. One end of each torsion beam is connected to the mirror and the other is connected to the arm while the other ends of the arms are connected to the frame. Vibration of two pairs of arms and beams generates the tilting force on the mirror. Arm has two parts: main arm and sub-arm. Since sub-arm has a smaller length shrinking of the device size is achieved.

Forces and resulting torques acting on the fast scan mode of the design with sub-arms and pair of inner and outer beams are given in Figure 2.6. Considering the inner

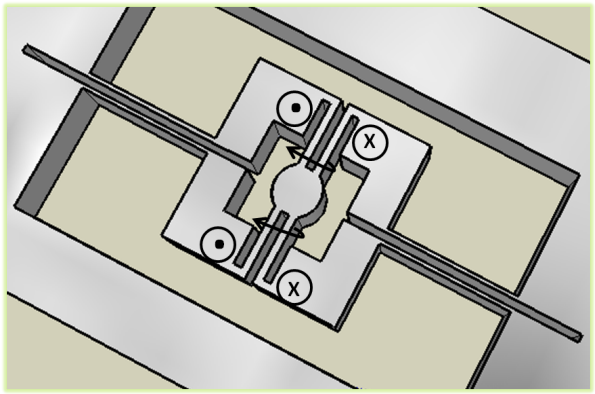

Figure 2.6. Effective forces on the fast scan mode of design with sub-arms and pair of outer and inner flexures.

beams in one side of the inner mirror, one of the beams experiences in-plane force while the other one is under the influence of out-of-plane force. The same situation applies to the the beams at the other side in a mirrored fashion the slow-scan axis being the axis of symmetry. This cause the inner mirror to give the desired mode for the horizontal scan. Simulation of the fast scan mode given in Figure 2.7 clearly shows the described behavior.

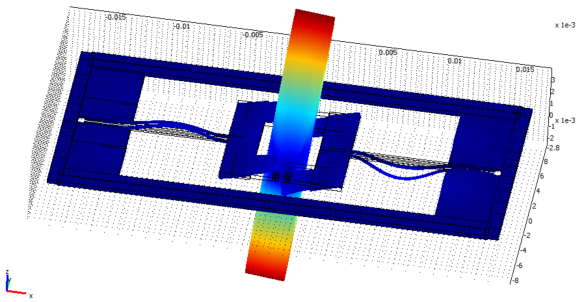

Figure 2.7. Simulation of the fast scan mode of the design with sub-arms and pair of outer and inner flexures.

The same mechanism works for the design with sub-arms and pair of inner beams as shown by its fast scan mode simulation given in Figure 2.8. However, the outer frame is more stable at the fast scan mode in the design with a pair of outer beams. The effect of pair of outer beams can be seen in the synchronization of the outer corner movements

with the corners next to arms of the outer frame.

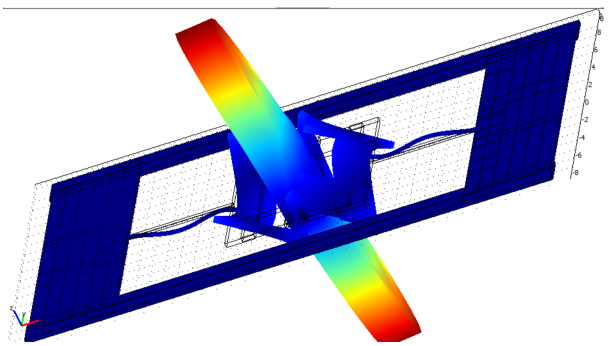

Figure 2.8. Simulation of the fast scan mode of the design with sub-arms and pair of inner flexures.

3. MECHANICAL BEHAVIOR OF RESONANT SCANNERS

Behavior of a beam mainly depends on its cross-sectional moment of inertia and the type of its support.

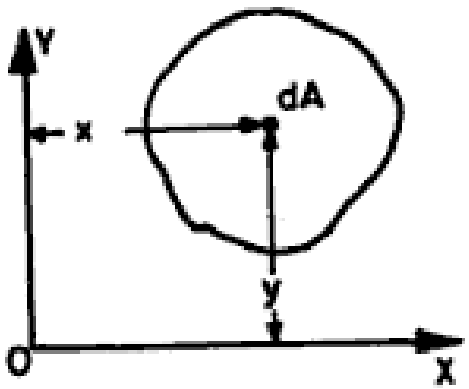

Figure 3.1. Area element for moment of inertia calculation.

For the area shown in Figure 3.1, the moment of inertia about x-axis is

$$I_{xx} = \sum y^2 dA \tag{3.1}$$

while the moment of inertia about y-axis is

$$I_{yy} = \sum x^2 dA \tag{3.2}$$

and the moment of inertia about z-axis is

$$J_z = I_{zz} = \sum (x^2 + y^2) dA = I_{xx} + I_{yy} \tag{3.3}$$

where dA is the elemental area with coordinates x and y. The moment of inertia about the axis perpendicular to the plane of the area, J_z in this case, is particularly called the 'polar moment of inertia'.

Since moment of area is xdA, the term x^2dA can be called 'second moment of area' as an alternative to moment of inertia. The moment of inertia of a plane area determines the strength of elements subject to bending. Thus, moment of inertia is a critical measure in fields such as structural design and strength of materials.

There are four types of beam end support: fixed, free, guided, and simply supported. Table 3.1 explains these types in terms of ability to rotate and/or translate.

Table 3.1. Beam End Support Types.

Support Type	**Translation**	**Rotation**
Free	✓	✓
Simply Supported	×	✓
Guided	✓	×
Fixed	×	×

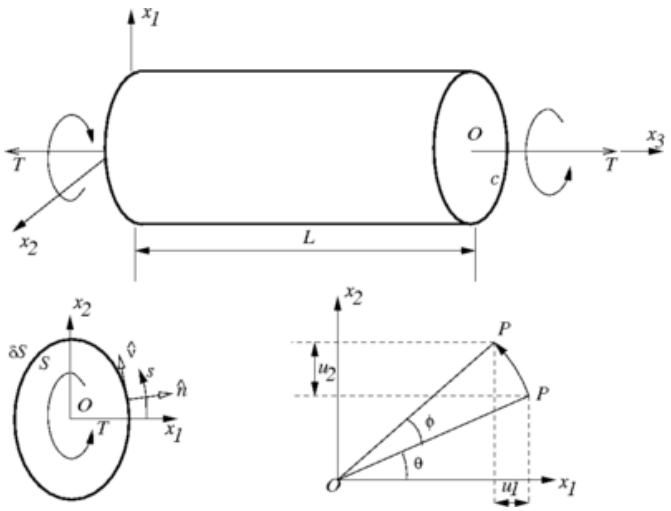

Figure 3.2. A bar under torsion.

3.1. Torsion Mechanics for the Scanner

Torsion is the twisting of a structure due to an applied torque. Consider a bar with length L_f shown in Figure 3.2 experiencing torsion under two end torques of T applied in the opposite directions to each other at each end. According to Saint Venant theory of uniform torsion, angle of rotation of a torsion bar is given by

$$\theta = \frac{TL_f}{GJ} \tag{3.4}$$

where G is the torsional modulus and J is the polar moment of inertia. Torsional spring constant is given by

$$K_s = \frac{T}{\theta}. \tag{3.5}$$

Since there are two non0circular torsion bars in proposed geometry,

$$K_s = \frac{2GK}{L_f}. \tag{3.6}$$

.

For a one-degree-of-freedom vibrating system with lumped mass in which the spring only gives the stiffness and the mass only gives the inertia, the equation-of-motion can be written as

$$\frac{d^2\theta}{dt^2} + \omega^2\theta = T. \tag{3.7}$$

For the gimbal-mounted bi-axial scanner (torsional scanner) geometry shown in

Figure 3.3 the fundamental resonant frequency is given by

$$f_{res} = \frac{1}{2\pi}\sqrt{\frac{K_f}{J_{eff}}} \tag{3.8}$$

where K_f is the flexural stiffness and J_{eff} is the effective mass moment of inertia.

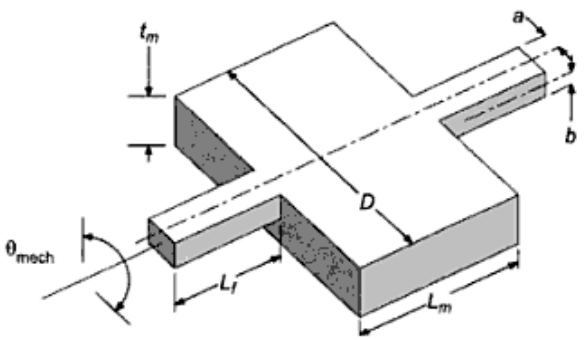

Figure 3.3. Gimbal-mounted biaxial scanner geometry. After [3].

Using Equation 3.8 and 3.6,

$$J_m\frac{d^2\theta}{dt^2} + \frac{2GK}{L_f}\theta = T \tag{3.9}$$

For a solid rectangular cross-section with dimensions $2a$ and $2b$ of an isotropic material with the condition that $a \geq b$, torsional stiffness is [36]

$$K = ab^3\left[\frac{16}{3} - 3.36\frac{b}{a}\left(1 - \frac{b^4}{12a^4}\right)\right] \tag{3.10}$$

Since steel is isotropic, this formula can be used for the outer and inner flexures with rectangular cross-section of proposed device geometry in Figure 2.1.

The mass moment-of-inertia of a rectangular mirror [37]

$$J_m = \frac{M_m}{12}\left(D^2 + t_m^2\right) \tag{3.11}$$

where M_m is the mass, D is the mirror size, and t_m is the thickness of the mirror.

For the inner frame, the mass moment-of-inertia of a circular mirror [37]

$$J_m = \frac{M_m}{12}\left(\frac{3}{4}D^2 + t_m^2\right) \tag{3.12}$$

where M_m is the mass, D is the diameter, and t_m is the thickness of the mirror.

The effective mass moment-of-inertia for the torsional mirror should involve the effect of flexures:

$$J_{eff} = J_{m,xx} + \frac{2}{3}J_{f,xx} \tag{3.13}$$

where $J_{f,xx}$ is the mass moment of inertia due to flexures and equal to

$$J_{f,xx} = \frac{1}{3}M_f\left(a^2 + b^2\right) \tag{3.14}$$

where M_f is the mass of one flexure.

The implementation of Roark's formulas [36] and vibration mode frequency formulae for torsional case [37] is done to the 2D scanner geometry with adding coupling terms for the inner mirror due to the mechanical coupling between outer and inner scanner structures. Tables given in Appendix A shows the results obtained with the analytical calculations.

3.2. Design Considerations

According to the formulas governing the mechanical behavior of 2D gimballed microscanner given in Section 3.1, the factors affecting the resonance frequencies can be listed as

- Cross-sectional geometry, thickness and width of the flexures determine the spring constant K.
- Properties of the structural material such as Young's modulus, torsional modulus, Poisson's ratio, and material density affect the torsional spring constant K_s and effective mass-moment of inertia J_{eff}.
- Number and orientation of flexures affect the spring constant. Designs with sub-arms and pair of beams offers shrinking in the size and increase in coupling between inner and outer mirrors.
- Geometric dimensions of the structure directly affect the mass moment of inertia and coupling between the inner and outer mirrors.
- Technology parameters directed by the fabrication method's capabilities affect the design geometry. Obligatory undercut openings in the etching mask and resolution restrictions in EDM have to be considered during the device design.

In the design of 2D selectively-thinned steel scanners an outer flexure torsion at about 200 Hz as the first vibrational mode is aimed for the slow-scan. For the fast-scan, inner flexure torsions at about 8 kHz and 16kHz with $\theta_{mech}D$ products of 3.9 and 7.8 deg·mm are targeted for QVGA and VGA applications, respectively. To achieve such a high ratio between fast and slow-scan frequencies, the outer flexures and inner mirror are thinned down. The thinning process provides a decrease in the spring constant of outer flexures and the mass moment-of-inertia of the inner mirror.

4. ACTUATION

4.1. Magnetic Actuation

In magnetic actuation there are two main sources for the magnetic field: current-carrying coil and/or permanent magnet. Table A.3 lists the major characteristics for different magnetic actuation mechanisms [3].

Table 4.1. Main magnetic actuation mechanisms.

Actuation Type	**Physical Mechanism**
Magnetostatic	Attraction between permanent magnet and ferromagnetic part
Electromagnetic	Attraction/repulsion between permanent magnet and electro-magnet
Lorentz Force	Force on a current-carrying conductor in a magnetic field
Magnetostriction	Dimensional change of magnetic material when magnetized

The magnetic force a charge experiences under an external magnetic field is called the Lorentz force and given by the formula

$$\vec{F} = Q\left(\vec{\nu} \times \vec{B}\right) \tag{4.1}$$

where Q is the total charge, ν is the velocity of the charge, and B is the magnetic field density. For line currents (wires)

$$\vec{F} = \int \left(\vec{\nu} \times \vec{B}\right)\, dq = \int \left(\vec{\nu} \times \vec{B}\right)\, \lambda\, \vec{dl} \tag{4.2}$$

where λ is the line current density. Since current through the wire is $I = \lambda\nu$, force on a current carrying wire becomes

$$\vec{F} = \int \left(\vec{I} \times \vec{B}\right) \, \vec{dl} \tag{4.3}$$

Since $\vec{I}$ and dl are always in the same direction for a wire,

$$\vec{F} = I \int \left(\vec{dl} \times \vec{B}\right) \tag{4.4}$$

For uniform magnetic field,

$$\vec{F} = I \left(\vec{L} \times \vec{B}\right) \tag{4.5}$$

The relationship between magnetic field density B and magnetic field H is given by the formula in MKS system

$$B = \mu_0 \left(H + M\right) \tag{4.6}$$

where $\mu_0 = 4\pi \ 10^{-7}$ is the permeability of free space and M is the magnetization. Magnetization is

$$M = m/V \tag{4.7}$$

where m is the magnetic moment and V is the volume of the material. m depends on magnetic properties of the material like the direction of magnetic moments of the spinning electrons and the orbital motion of electrons.

Susceptibility is defined as

$$\chi = \frac{M}{H}. \tag{4.8}$$

Thus, relative permeability which is $\mu_r = B/H$ becomes

$$\mu_r = 1 + \chi. \tag{4.9}$$

Materials are classified in terms of their response to magnetism according to the their relative permeability values as follows

- If $\mu_r < 1$, material is "diamagnetic".
- If $\mu_r > 1$, material is "paramagnetic".
- If $\mu_r >> 1$, material is "ferromagnetic".

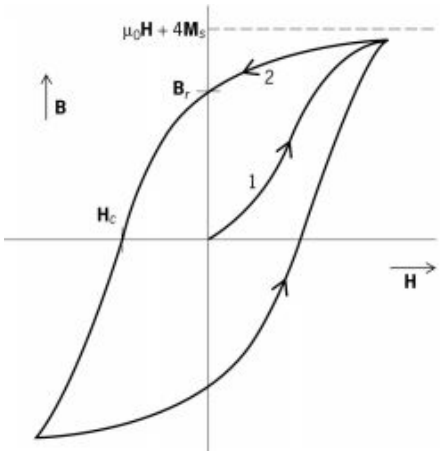

Figure 4.1. A typical magnetization curve.

Magnetic properties of materials play an important role in designing a magnetically actuated microsystem. Magnetic susceptibility, the magnetization curve, and magnetic domains in ferromagnetic materials need to be considered. Magnetization curve shown in Figure 4.1 is the graph of magnetization (M) versus magnetic field (H) of a material. From a magnetization curve five important parameters can be deduced: the saturation magnetization M_s), coercive field (H_c), remanent magnetization (M_r), energy product $(BH)_{max}$, and hysteresis. Ferromagnets' B-H curve shows 'hysteresis' while others have linear B-H curves. Magnetic materials are divided into two categories according to their

coercive field value: soft and hard magnets. Soft magnets are easier to magnetize, have smaller H_c and cannot retain their magnetization as good as hard magnets.

4.2. Ferromagnetism

Magnetization of ferromagnetic materials saturates above a certain magnetic field value. Their susceptibility and relative permeability are large, positive, and functions of the applied field, H. They consist of magnetic domains which are small regions with uniform magnetization. Figure 4.2 shows the magnetic domains. In the absence of external magnetic field, directions of magnetization of domains show randomness. When an external field is applied, domains favoring the orientation of external field grow while others shrink.

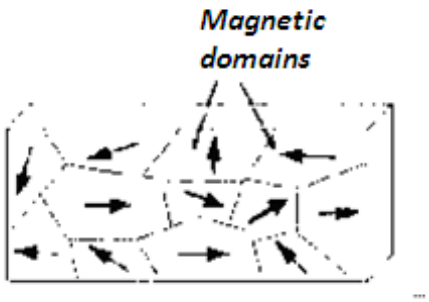

Figure 4.2. Magnetic domains.

4.3. Moving Magnetic Material Actuation

Maxwell's equations governing the magnetism are

$$\nabla \cdot B = \nabla \cdot (\mu_0 H + M) \tag{4.10}$$

$$-\nabla \cdot M = \mu_0 \nabla \cdot H = \eta_m \tag{4.11}$$

where η_m is the magnetic charge density. Total magnetic charge φ can be found by

$$\varphi = \int_v \eta_m dv = MS \tag{4.12}$$

where S is the pole surface.

Force induced on a magnetic pole is given by

$$F = \varphi H = MSH. \tag{4.13}$$

When a magnetic material is placed inside a uniform magnetic field with an angle ϕ , a torque T is generated

$$T = \varphi Hl \sin \phi = MHV \sin \phi \tag{4.14}$$

Corresponding magnetostatic energy is given by

$$U_{ms} = -V\vec{H} \cdot \vec{M} = -VHM \cos \phi \tag{4.15}$$

4.3.1. Torsional Electromagnetic Actuation

In devices with a torsion beam supporting a plate, torque generated by external magnetic field cause the plate to rotate out-of-plane as shown in Figure 4.3. A magnetic sample with a net magnetization $\vec{M}$ in an external magnetic field $\vec{H}$, experiences a torque $\vec{T}_{field}$ [4]

$$T_{field} = V_{mag}|\vec{M} \times \vec{H}| = V_{mag}MH \sin \alpha \tag{4.16}$$

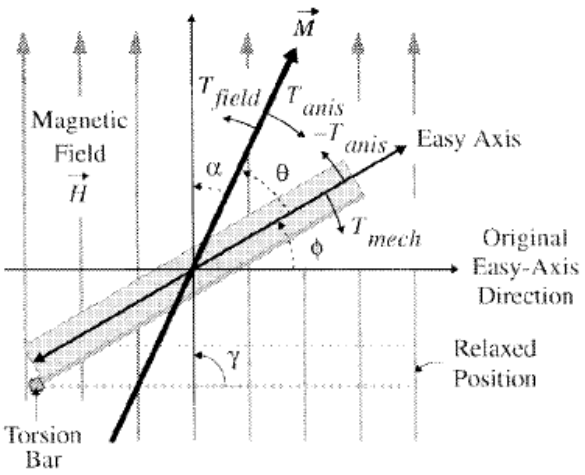

Figure 4.3. Magnetization actuation principle. After [4].

where V_{mag} is the magnet volume and α is the angle between $\vec{M}$ and $\vec{H}$. The equilibrium direction for the torque is the 'easy axis' of the sample. When the torque T_{field} rotates $\vec{M}$ an angle θ away from the easy axis a magnetic anisotropy torque T_{anis} given by

$$T_{anis} = -K_{anis} \sin 2\theta \tag{4.17}$$

where K_{anis} is called the magnetic-anisotropy constant, tries to realign $\vec{M}$ with the easy axis. As opposed to T_{anis} an equal but opposite torque $-T_{anis}$ is exerted in the direction of easy axis If the flexure of the magnetic sample has an angular spring constant k_ϕ, $-T_{anis}$ will cause the magnetic sample to rotate an angle ϕ from its original orientation generating the mechanical restoring torque

$$T_{mech} = -k_\phi \phi \tag{4.18}$$

If the direction of external magnetic field remains at a constant angle γ to the original direction of the easy axis,

$$T_{field} = V_{mag} M H \sin(\gamma - \theta - \phi). \tag{4.19}$$

In equilibrium, the field torque T_{field}, which rotates M away from the easy axis, is balanced by the anisotropy torque T_{anis} , which acts to align M with the easy axis. In turn, the torque on the magnetic material $-T_{anis}$ is balanced by T_{mech}. The resulting equilibrium condition is $|T_{field}| = |T_{anis}| = |T_{mech}| = T$. This can be solved by equating the given formulas with M known [4].

The dynamic torsion model for this system is given by

$$J\ddot{\Phi} + C_{\Phi}\dot{\Phi} + k_{\Phi}\Phi = T_{field} \tag{4.20}$$

where J is the angular moment of inertia of the magnetic mirror, k_{Φ} is the angular stiffness of the torsional beam, C_{Φ} is the angular damping coefficient and given by

$$C_{\Phi} = \sqrt{\frac{Jk_{\Phi}}{Q}} \tag{4.21}$$

where Q is the quality factor. Due to shape anisotropy magnetization can be assumed to be along the easy axis, $\theta = 0$, and if γ is assumed to be 90°, the field torque becomes

$$T_{field} = V_{mag}M(H_{dc} + H_{ac}\sin 2\pi ft\cos\Phi). \tag{4.22}$$

From Equation 4.20, 4.21, and 4.22 driving frequency(f) can be expressed in terms of rotation angle (Φ) .

5. FABRICATION

Two main methods are employed in the fabrication of proposed devices: electrochemical etching with single mask photolithography and electric discharge machining (EDM).

5.1. Electrochemical Micromachining

Electrochemical etching is one of the methods to be used for the micromachining of metals. The method proposed in [5] enables the fabrication of the structures with different thicknesses on the same substrate by using the 'etch lag' principle. Etch lag refers to the direct proportionality between aspect ratio of a feature and the required time to etch it through. In other words, small openings tend to etch more slowly than larger ones. To make use of this principle, openings defining the parts to be thinned give slower etch rates than all the other openings. To thin down the inner mirror and outer flexures of the device, proposed fabrication scheme shown in Figure 5.1 is used. Figure 5.2 depicts the change in the process profile for small and bigger openings in the mask.

In drawing the etch masks, several points should be considered [5]:

- For dimensions smaller than 500 μm, the etching process becomes mass transport limited. Refreshing of chemical reactants and removal of by-products are harder for smaller dimensions, thus etch rate decreases.

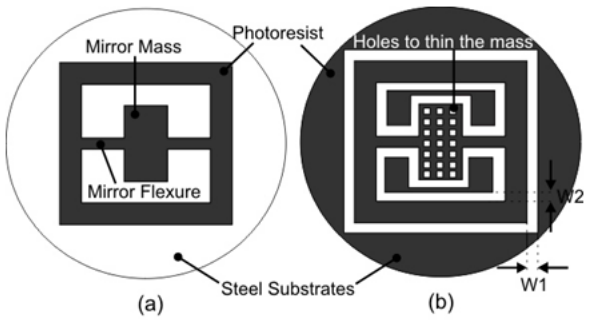

Figure 5.1. Proposed masking scheme to thin the device. After [5].

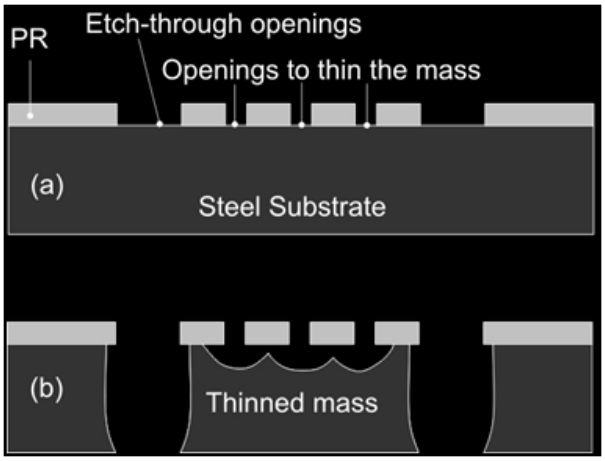

Figure 5.2. Etching profile of steel substrate. After [5].

- Electrical field at the edges are stronger than the ones in the middle. Etch rate at the edges are bigger than the rest of the etched areas.
- For dimension bigger than the optimum value, the edge effect becomes negligible. For bigger dimensions, this effect decreases and the etch rate in the middle of the openings becomes dominant.

5.1.1. Etch Tests

Two different electrolytic solutions are used: hydrogen chloride (HCl) and sodium chloride (NaCl). Process parameters should be known in order to be able to draw the photolithographic masks defining the structures. Figure 5.3 shows the etch depth values for different mask openings and Figure 5.4 plots the anisotropy for various current density values for HCl etching.

For NaCl etch process characterization, some test masks are drawn and after photolithographic process, SS 420 test structures are formed using NaCl etch. Figure 5.5 shows the etch depth for openings at various dimensions at various current densities. Figure 5.6 gives the anisotropy values.

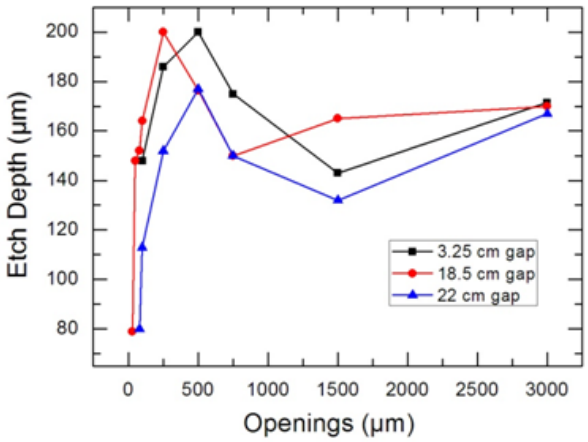

Figure 5.3. HCl etch depth for different mask openings. After [5].

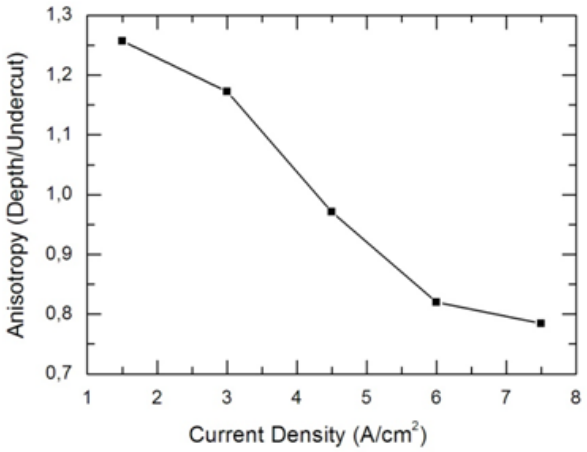

Figure 5.4. Anisotropy vs. current density for HCl etch. After [5].

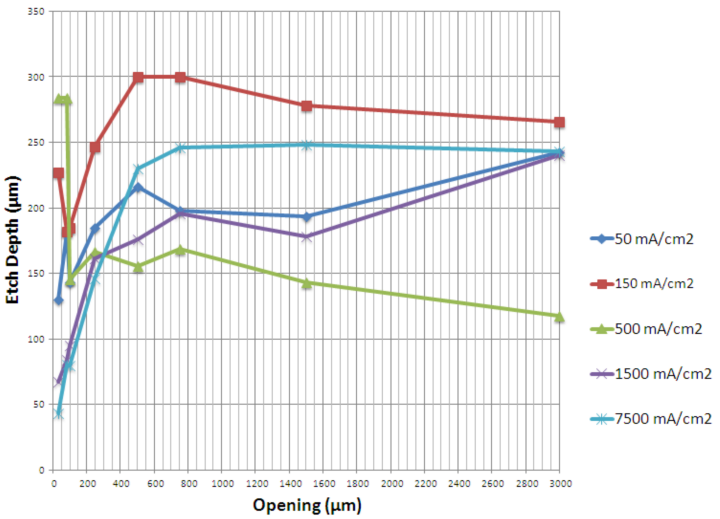

Figure 5.5. Etch depth graph for NaCl etch.

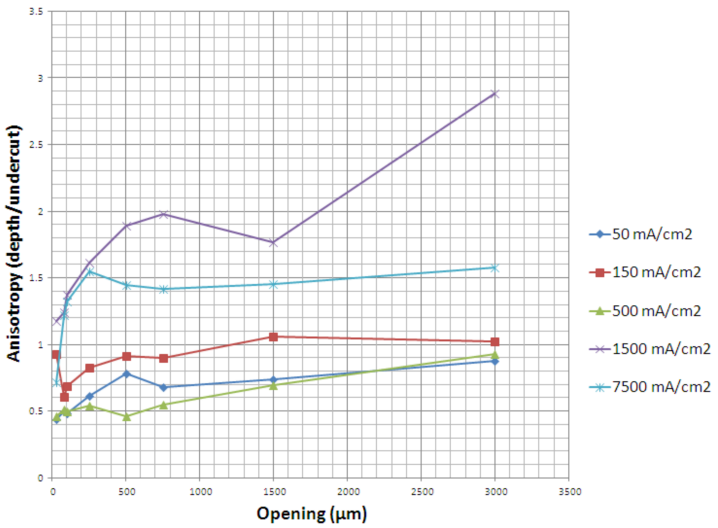

Figure 5.6. Anisotropy graph for NaCl etch.

5.1.2. Photolithographic Process

A photoresist mask is patterned on the surface of the steel substrate before the etching process. A 300 μm SS 420 substrate is first cleaned with acetone and IPA. After a dehydration bake at 120° C for 5 minutes the substrate is spin coated at 2000 rpm with a 6 μm thick Shipley 1828 photoresist. After a soft-bake at 90° C for 1 minute, the steel substrate is exposed to UV light for 90 seconds at 490 Watts. Development of the photoresist is done in MF-26A developer for 90 seconds. Hard-bake is done at 130 textsuperscripto C for 1 hour and at 110° C for 2 hours, successively. Time of the hard-bake is kept long on purpose since it increases the durability of the PR mask during the electrochemical etch.

5.1.3. Etching

Figure 5.7 depicts the setup used for the electrochemical etching process. The structure to be etched is connected as the anode whereas the counter plate, made out of steel, to collect the resultant ions is the cathode. A DC power supply is connected between anode and cathode in order to provide the current to the system. For HCl etching, a current density of 3 A/cm^2 is used with an electrode gap of 3.25 cm for 5 minutes while for NaCl 7.5 A/cm^2 is used for 10 minutes with a gap of 28 cm.

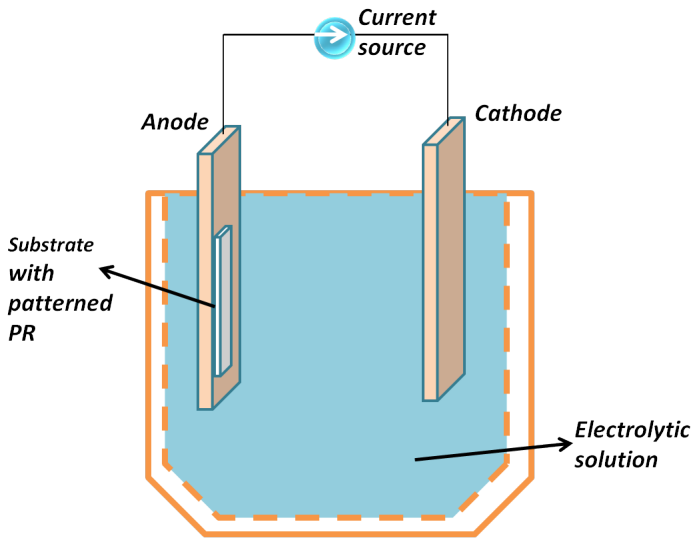

Figure 5.7. Electrochemical Etch Setup.

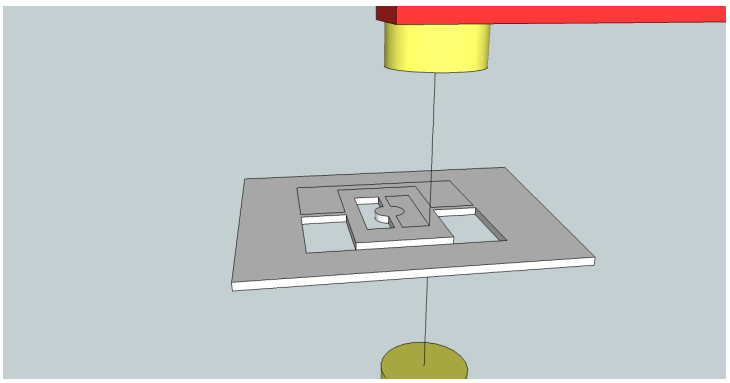

Figure 5.8. Wire EDM.

5.2. Electric Discharge Machining

Electrical discharge machining, abbreviated as EDM, is a versatile and high-precision machining technique for the fabrication of electrically-conductive mechanical components. Due to the high potential difference applied between the tool and the workpiece, an electrical spark is generated. In EDM, shape is given to the workpiece by using the large localized heat flux resulting from this spark. Process is done inside a dielectric medium, deionized (DI) water in this case, in order to prevent the shorting of the system and flush the molten material removed with the suddenly and locally increased temperature.

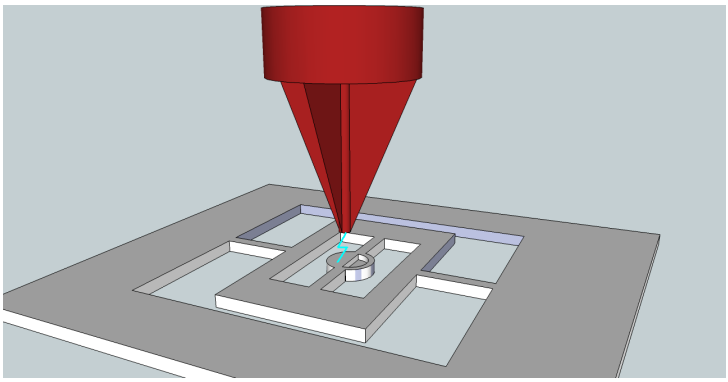

Figure 5.9. Sinker EDM.

In the fabrication process, two types of EDM techniques are used. Scanner contours are first defined by using wire-EDM process, as shown in Figure 5.8. Then back side of the mirror as well as the torsion beams connecting the gimbal frame to the anchors are thinned by using sinker-EDM process, shown in Figure 5.9. In wire-EDM, a brass wire is used to ablate unnecessary parts whereas in sinker EDM, sparks in the surface of the electrode are used to plunge a cavity of approximately 150 μm on targeted regions. Photograph of the fabricated structure is shown in Figure 6.14.

6. EXPERIMENTS AND RESULTS

6.1. Electropolish Experiments on SS 301 and SS 420 Substrates

Stainless steel substrates to be electropolished are sanded by using sandpapers of various grit sizes. Steel substrate to be polished is connected to the positive/anodic terminal while a conducting plate is connected to negative/cathodic terminal. Both are placed in $2H_3PO_4 : 1H_2SO_4 : 1$DI water which is the electrolytic solution specially chosen for the electropolishing of stainless steels. For five minutes, 0.5 Ampere DC current is applied per 1 cm^2 stainless steel area to be polished. Setup is shown in Figure 6.1.

Resulting SS 301 and SS 420 substrates are shown in Figure 6.2 and 6.3, respectively.

As clearly seen from the pictures, electropolishing experiments were successful in SS 301 but unsuccesful in SS 420. Two solutions are found in the literature:

- If stainless steels 420, 440A, 440B, or 440C are to be electropolished, they must first be annealed at 300-700^o F in order to avoid pickling cracks [38].
- The basic formulations for stainless steels are based on sulphuric acid and orthophosphoric acid, but these are generally not very successful with 400 series, so extra additives such as hydroacetic acid and/or aryl sulphonic acids are used [39].

6.2. 2D Gimbal Steel Scanner - First Iteration

Four different structures are designned as the first iteration.

In these designs, rib and rim as shown in Figure 6.4 are included on thinned down parts in order to increase the mechanical strength of the structure.

Figure 6.6 and 6.7 show the masks for photolithographic process. Masks are de-

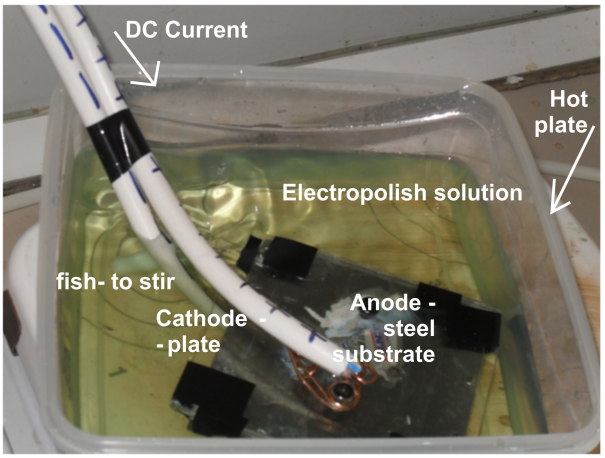

Figure 6.1. Electropolish setup for stainless steel.

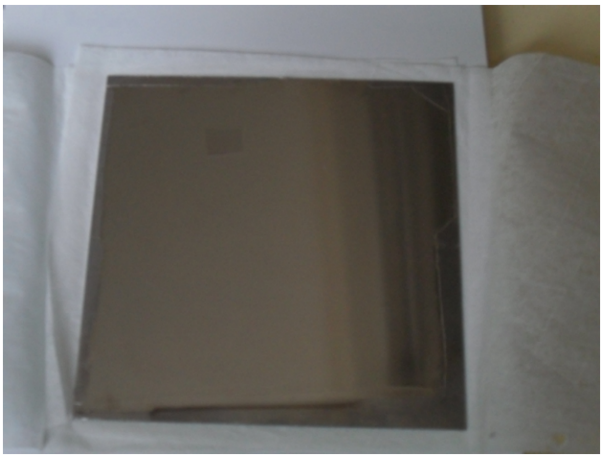

Figure 6.2. SS 301 substrate after electropolishing process.

Figure 6.3. SS 420 substrate after electropolishing process.

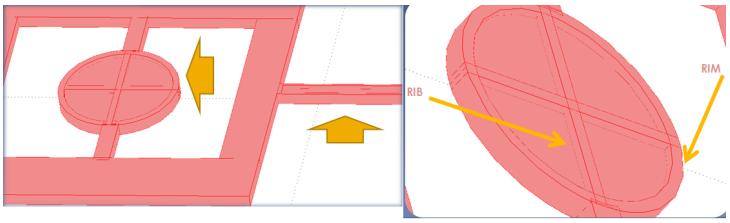

Figure 6.4. (a) Parts to be thinned down (b) Rib and rim.

signed for HCl etch. For the thinning parts two types of opening schemes are used for the same design as shown in Figure 6.5.

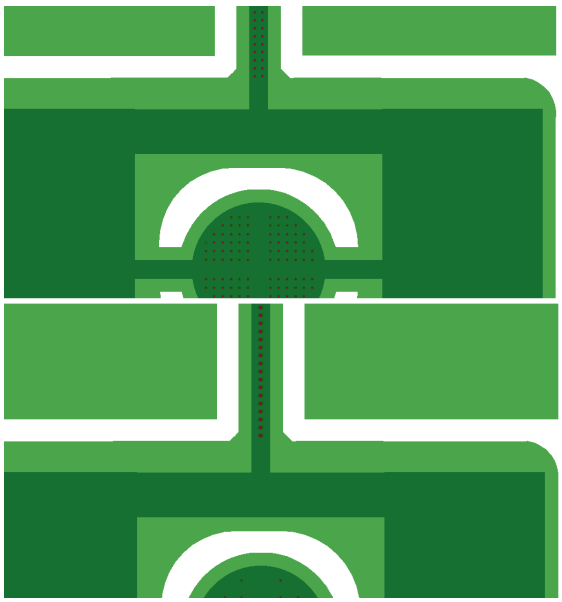

Figure 6.5. (a) Thinning with smaller and more number of openings (b) Thinning with larger and less number of openings.

HCl etching is used with currents of 21.84 A and 21.52 A for the first and second photolithographic masks, respectively. Photograph of the fabricated scanner is shown in Figure 6.8. Figure 6.9 shows the slow scan TOSA vs frequency and Figure 6.10 shows the fast scan TOSA vs frequency of the scanner.

A slow scan TOSA of 144.31° is achieved at 54 Hz at 405 mW. Fast scan TOSA is 0.009° at 15040 Hz for 88.2 mW input power.

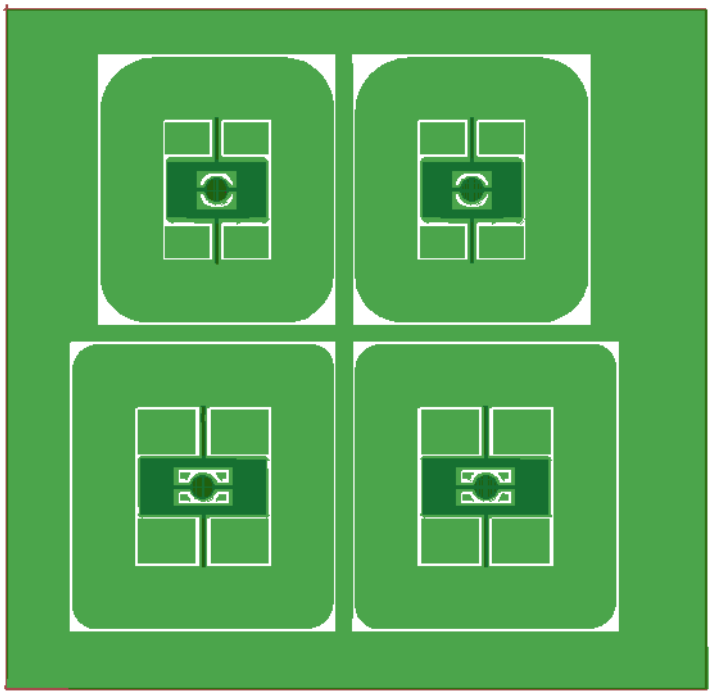

Figure 6.6. Photolithographic mask-1 for the first iteration.

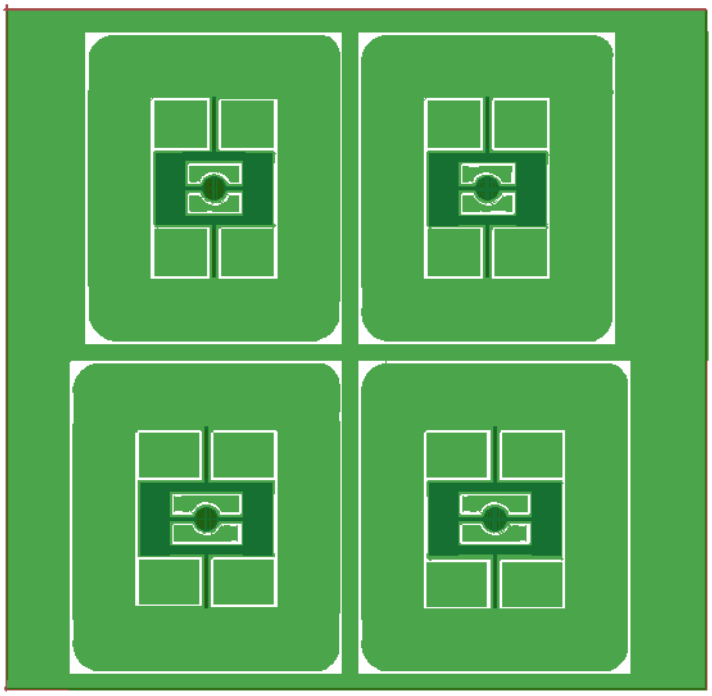

Figure 6.7. Photolithographic mask-2 for the first iteration.

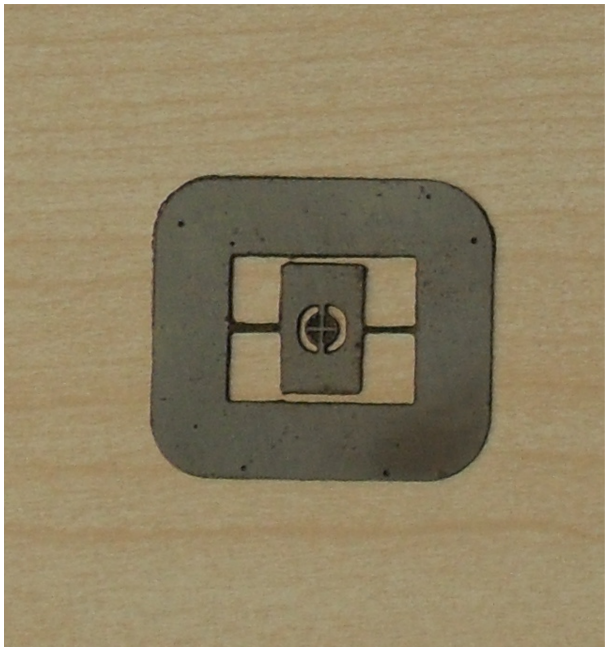

Figure 6.8. Photograph of the first fabricated scanner.

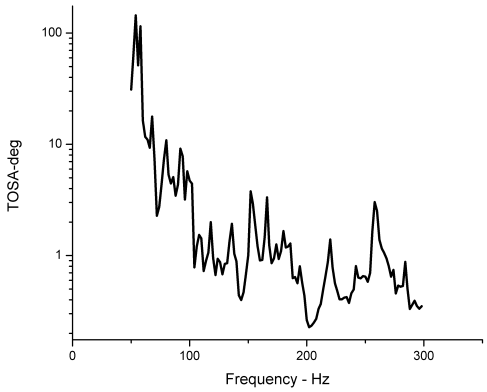

Figure 6.9. TOSA plot of slow scan for the first scanner.

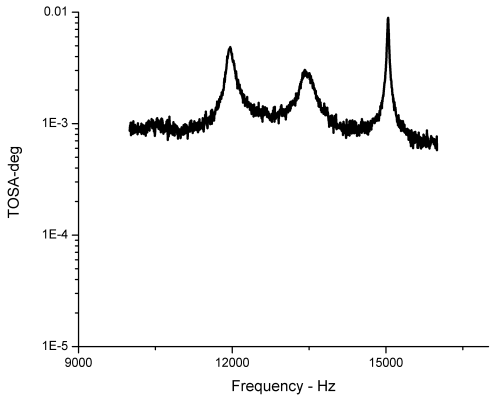

Figure 6.10. TOSA plot of fast scan for the first scanner.

Since the inner beams are not long enough in the design, resulting fast scan TOSA is inadequate for QVGA standards, a new design iteration starts.

6.3. 2D Gimbal Steel Scanner - Second Iteration

In order to improve the displacement of the inner mirror, inner flexures are designed to be longer this time. NaCl solution is desided to be used as the etchant to improve the roughness of the sidewalls. Therefore, NaCl etch process characterization is done in order to determine the parameters for the photolithographic mask. Results of these test are given in Section 5.1.1. Mask for the second iteration design is shown in Figure 6.11.

During the fabrication there were difficulties related to the by-products. Fabricated structures were very rough. Photograph is given in Figure 6.12.

6.4. Selectively Thinned Steel Scanners Using Electrical Discharge Machining

The designs given in Section 6.2 are also manufactred using EDM. Drawing in .dxf format used in the process is shown in Figure 6.13.

Scan lines of the fabricated scanner are given in Figure 6.15, 6.16, and 6.17 . The

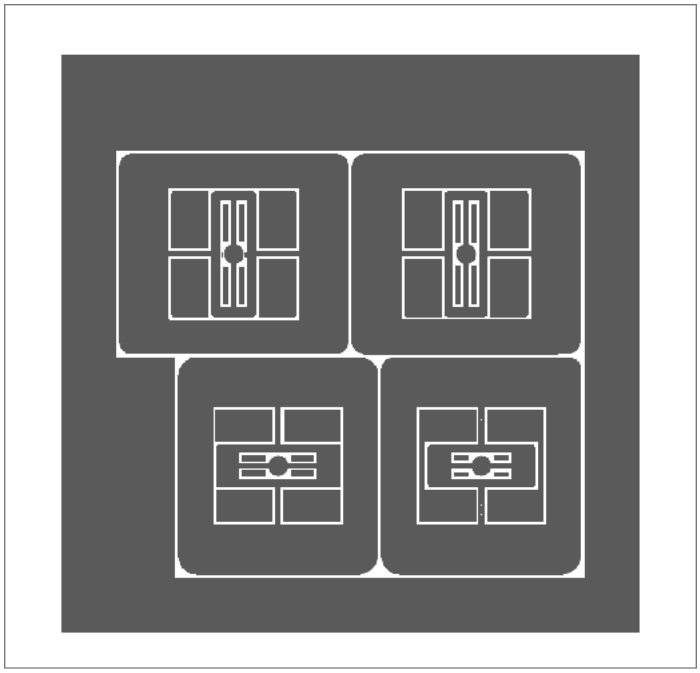

Figure 6.11. Photolithographic Mask for Second Design Iteration.

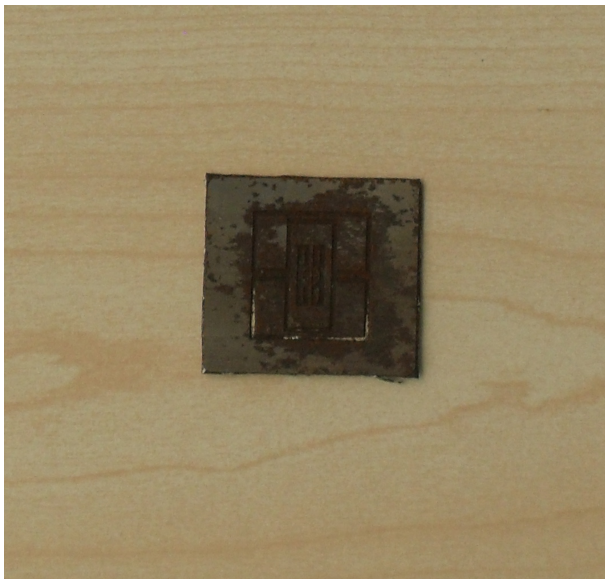

Figure 6.12. Photograph of the second iteration scanner fabricated by NaCl etching.

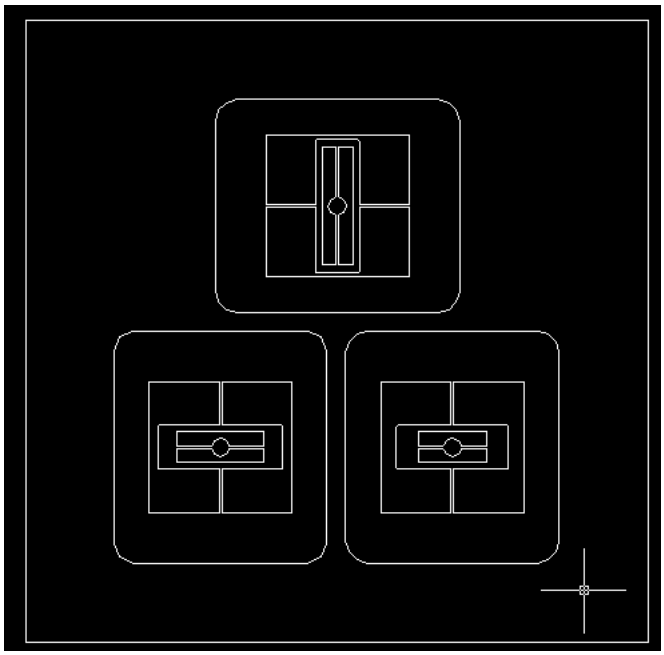

Figure 6.13. Drawing for EDM.

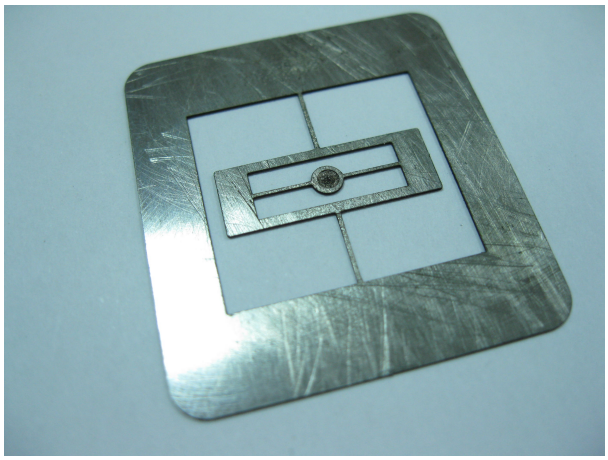

Figure 6.14. Fabricated 2D gimbal mounted EDM scanner.

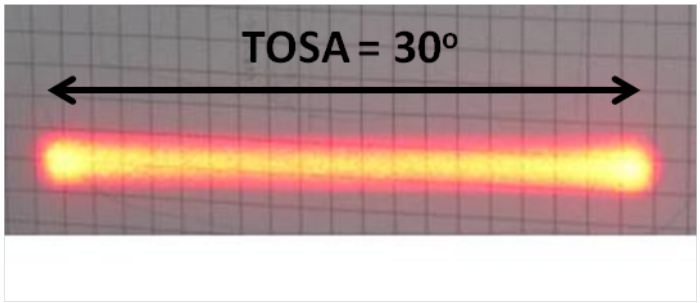

Figure 6.15. Slow scan line of the fabricated 2D gimbal mounted EDM scanner.

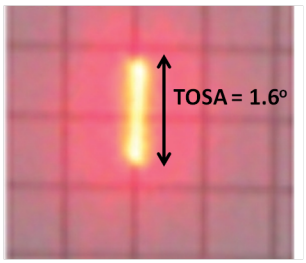

Figure 6.16. Fast scan line of the fabricated 2D gimbal mounted EDM scanner.

scan line generated by the slow-scan motion of the scanner corresponds to 30° at a drive power of 160 mW. The maximum slow scan total optical scan angle is measured to be 78° at 222 mW, as shown in Figure 6.18. The scan line generated by the fast-scan motion corresponds to 1.6° at 10875 Hz with 435 mW drive power.

Figure 6.19 plots the peak displacements and corresponding resonance frequencies of the actuator for different drive levels.

6.4.1. Nickel Electroplated EDM Scanner

The scanner fabricated with EDM is electroplated with nickel which is also a ferromagnetic material. Resulting scanner is shown in Figure 6.20. The scan lines generated using this scanner are shown in Figure 6.21. The scan line generated by the fast-scan

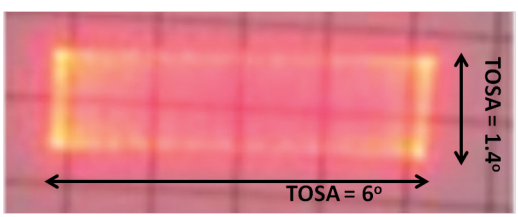

Figure 6.17. 2D raster scan of the fabricated 2D gimbal mounted EDM scanner.

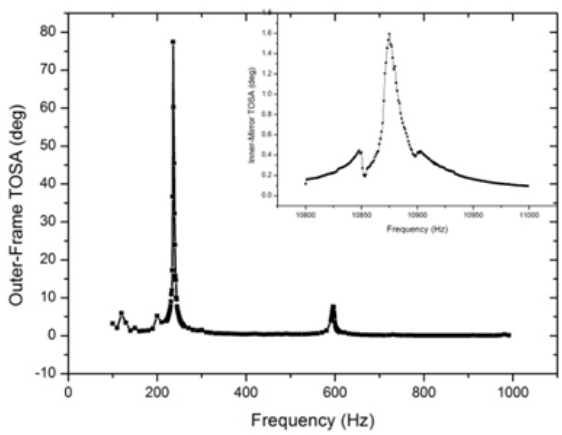

Figure 6.18. TOSA plot of outer-frame and inner-mirror (inset) vs. frequency of the fabricated 2D gimbal mounted EDM scanner.

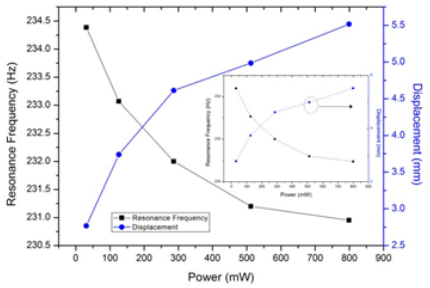

Figure 6.19. Driving Power vs. resonance shift and displacement plots of both scan mirror and outer frame (inset) of the fabricated 2D gimbal mounted EDM scanner.

motion corresponds to a TOSA of 8° at 11271 Hz at 65 mW power.

Figure 6.20. Photograph of the nickel electroplated 2D gimbal mounted EDM scanner.

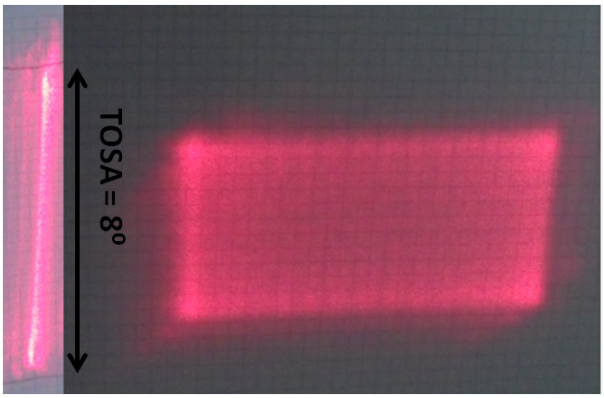

Figure 6.21. (a) Fast scan line (b) 2D raster scan of the nickel electroplated EDM scanner.

6.5. Designs with Sub-Arms and Pair of Beams

New designs with subarms and pair of beams are designed and their drawing in .dxf format shown in Figure 6.22 is sent for EDM fabrication.

The design with subarms in Figure 6.23 achieved a slow scan TOSA of 58.007° at 190 Hz at 353 mW as shown in Figure 6.24.

A fast scan TOSA of 4.62° at 3654 Hz for 65 mW power is achieved as shown in Figure 6.25.

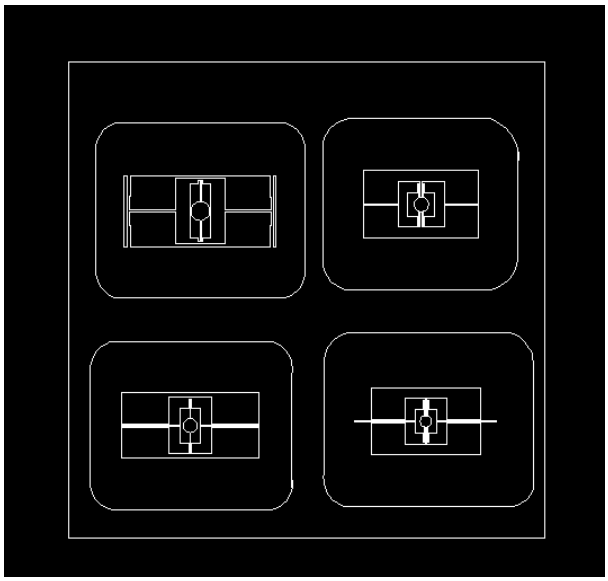

Figure 6.22. EDM drawing for the designs with sub-arms.

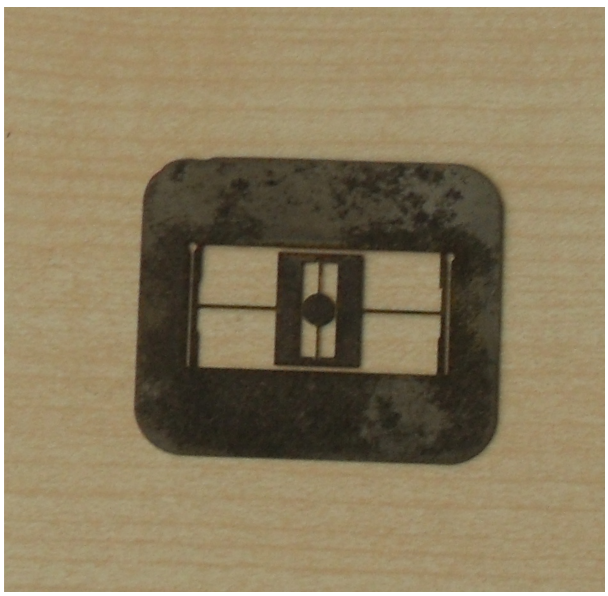

Figure 6.23. Photograph of the design with sub-arms.

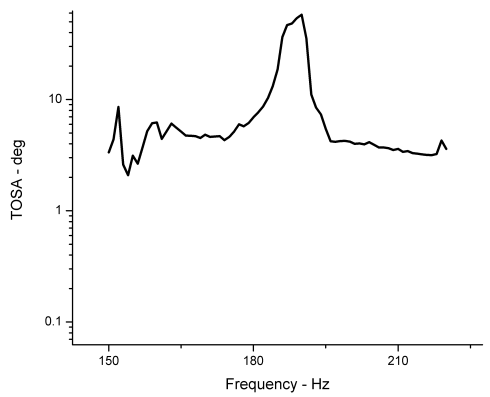

Figure 6.24. Slow scan response of design with sub-arms.

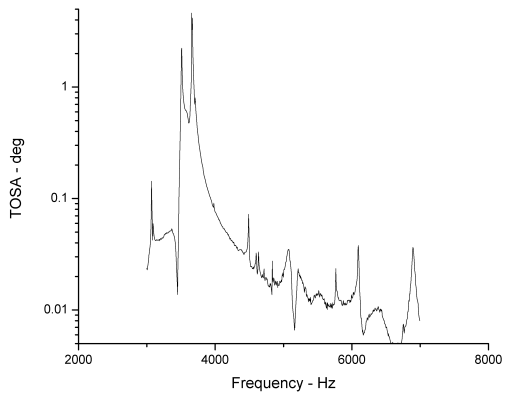

Figure 6.25. Fast scan response of design with sub-arms.

The design with subarms and pair of outer flexures in Figure 6.26 achieved a slow scan TOSA of 63.746° at 199 Hz for 353 mW power as shown in Figure 6.27.

Figure 6.26. Photograph of the design with sub-arms and pair of outer flexures.

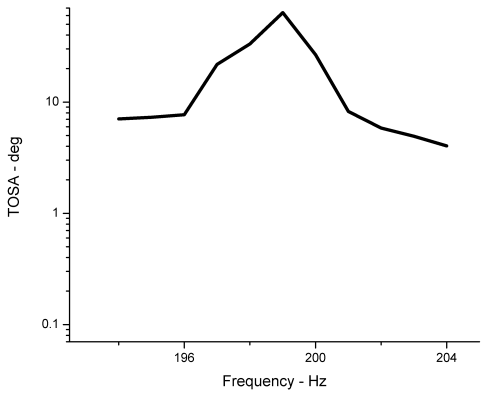

Figure 6.27. Slow scan response of design with sub-arms and pair of outer flexures.

A fast scan TOSA of 1.125° at 5732.7 Hz for115 mW power is achieved as shown in Figure 6.28.

The design with subarms and pair of inner flexures in Figure6.29 achieved a slow scan TOSA of 106.942° at 188.2 Hz for 353 mW power as shown in Figure 6.30.

A fast scan TOSA of 0.225° at 10970 Hz for 65mW power is achieved as shown in

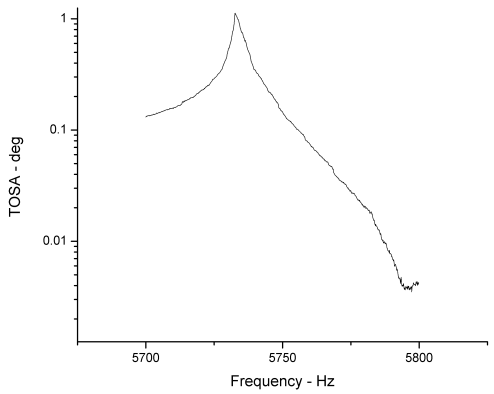

Figure 6.28. Fast scan response of design with sub-arms and pair of outer flexures.

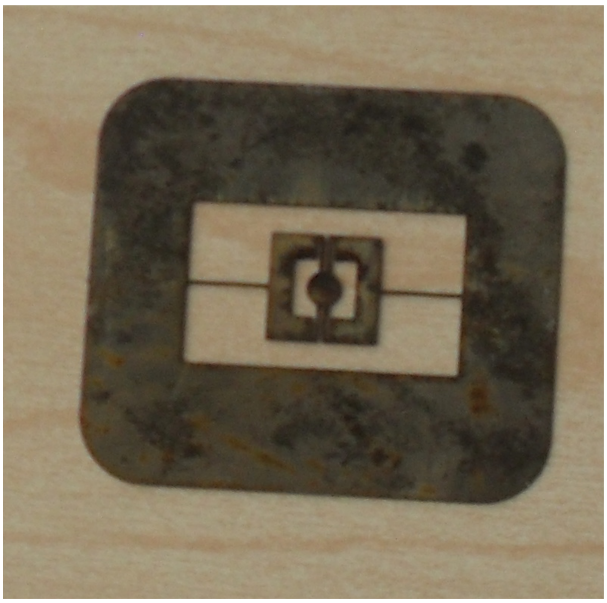

Figure 6.29. Photograph of the design with sub-arms and pair of inner flexures.

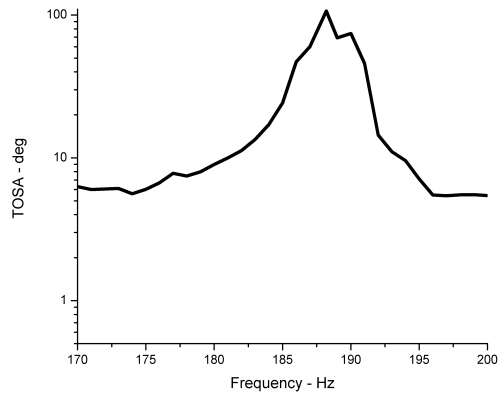

Figure 6.30. Slow scan response of design with sub-arms and pair of inner flexures.

Figure 6.31.

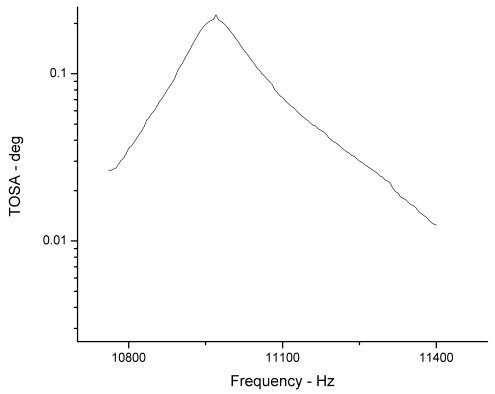

Figure 6.31. Fast scan response of design with sub-arms and pair of inner flexures.

The design with subarms and pairs of both inner and flexures in Figure 6.32 achieved a slow scan TOSA of 58.64° at 139 Hz for 384 mW power as shown in Figure 6.33.

A fast scan TOSA of 0.046° at 28085 Hz for 38 mW power is achieved as shown in Figure 6.34.

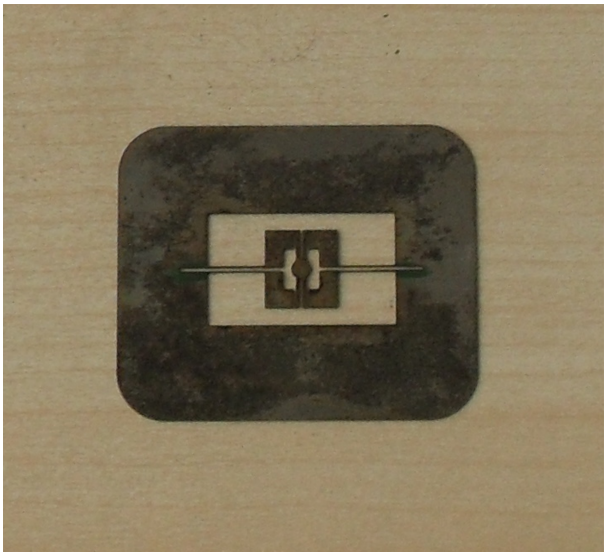

Figure 6.32. Photograph of the design with sub-arms and pairs of both inner and flexures.

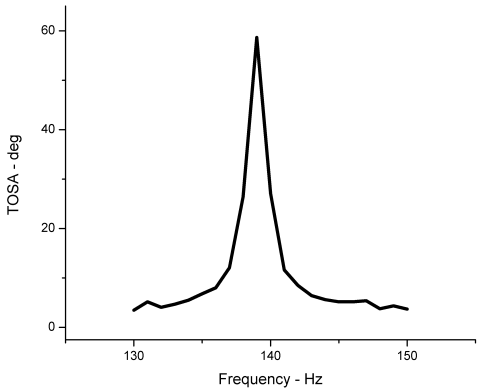

Figure 6.33. Slow scan response of design with sub-arms and pairs of both inner and flexures.

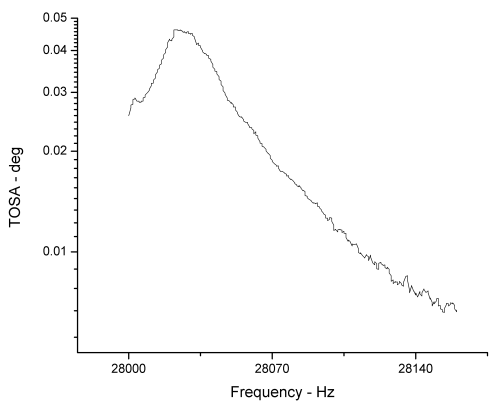

Figure 6.34. Fast scan response of design with sub-arms and pairs of both inner and flexures.

7. CONCLUSION

This thesis reports the design and fabrication of selectively thinned 2D steel scanners aimed to be used in projection display applications. 2D gimbal architecture is mainly employed with design variations in the number of parallel beams and adding sub-arms. Two main fabrication methods are employed in the manufacturing of devices: electrochemical micromachining and EDM. Electromagnetic actuation is used with an AC current-carrying coil and a permanent magnet.

Table 7.1 lists the results obtained with different design and fabrication methods. Current driving scheme proposed in [40] is used in the measurements except for design 2. For design 2, a current amplifier is used to amplify the signal from the signal generator. Some conclusions that can be drawn from these results are:

- Design 3.1 and Design 3.2 have relatively low fast scan frequencies due to the lack of the selective thinning.
- Design 3.4 achieved a high fast scan frequency of 28 kHz with the help of the sub-arms and doubling the number of beams both in inner and outer frames.
- Electroplating of nickel improves the performance by increasing the magnetization on the substrate since it is a ferromagnetic material.
- Electrochemical etching with HCl and EDM gives good results in shaping of the steel scanners. However, some additives should be tried in the NaCl solution in order to etch the 2D steel scanner geometry properly.
- Nickel electroplated Design 2 achieved the QVGA and VGA spec in terms of θD product. Design 3.1 achieved QVGA spec.

Combination of photolithographic process, electrochemical etching and EDM methods are planned as the future work. Selective thinning of the structures can be done by electrochemical etching while the ablation of the scanner by EDM. This combined method can give better results in terms of surface roughness and precision of dimensions.

Improvement in the actuation scheme current driving coil especially for high frequencies is essential for the actuation of mirrors above 10 kHz. For this purpose high frequency cores and different core geometries can be employed.

Table 7.1. Comparison of the performance of fabricated scanners.

	Thinned Parts	**Sub-arm**	**Outer Flex-ures**	**Inner Flex-ures**	**Fabrication**	**Slow Fre-quency (Hz)**	**Slow Scan TOSA (deg)**	**Power (mW)**	**Fast Fre-quency (Hz)**	**Fast Scan TOSA (deg)**	θD **(deg.mm)**	**Power (mW)**
Design 1	✓	×	1	1	Electro chemical	54	144.3	405	15040	0.009	0.007	88
Design 2	✓	×	1	1	EDM	236	78	222	10875	1.16	0.87	435
Design 2 Nickel	✓	×	1	1	EDM	285	82	304	11271	8	6	65
Design 3.1	×	✓	1	1	EDM	190	58	353	3654	4.62	4.62	146
Design 3.2	×	✓	2	1	EDM	199	63.7	353	5732.7	1.125	0.844	115
Design 3.3	×	✓	1	2	EDM	188.2	106.9	353	10970	0.225	0.169	65
Design 3.4	×	✓	2	2	EDM	139	58.64	384	28085	0.046	0.0296	38

APPENDIX A: EXCELSHEET

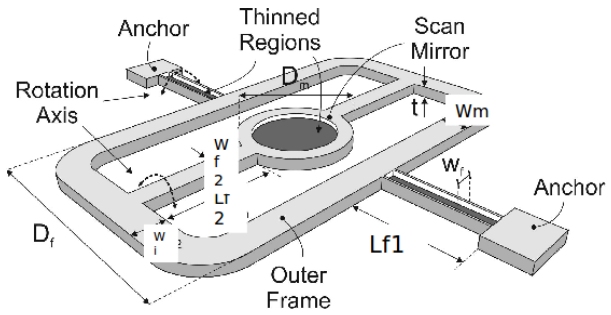

Figure A.1. Edges used in the analytical calculations for Design 2.

Table A.1. Inputs for the analytical calculations implemented on Design 2.

Edge	**Unit**	**Value**
L_{f1}	m	7e-03
W_{f1}	m	4e-04
W_m	m	1e-03
W_i	m	3e-03
L_{f2}	m	5e-03
W_{f2}	m	4e-04
L_{out}	m	2.3e-03
R_m	m	1.5e-03
T_t	m	2.5e-04
T_u	m	3e-04
G	N/m^2	8.07e+10
ρ	kg/m^3	7700

Table A.2. Outputs for the analytical calculations implemented on Design 2.

Edge	**Unit**	**Value**
K_{in}	m^4	1.94e-15
$M_{m,in}$	kg	1.36e-05
$K_{s,in}$	kgm^2/s^2	6.27e-02
$J_{m,xx,in}$	kgm^2	7.72e-12
$M_{f,in}$	kg	4.62e-06
$J_{f,xx,in}$	kgm^2	9.63e-14
$M_{m,coupling}$	kg	1.85e-04
Coupling coefficient	-	1.69e-04
$J_{eff,coupling}$	kgm^2	3.12e-08
$J_{eff,in}$	kgm^2	1.31e-11
K_{out}	m^4	1.273e-15
$K_{s,out}$	kgm^2/s^2	2.94e-02
$J_{m,xx,out}$	kgm^2	9.43e-09
$M_{f,out}$	kg	4.31e-06
$J_{f,xx,out}$	kgm^2	8e-014
$J_{eff,out}$	kgm^2	9.43e-09

Table A.3. Calculated, simulated and experimental resonance frequencies.

Edge	**Unit**	**Calculated**	**Simulated**	**Experimental**
$f_{res,in}$	Hz	11036.08	12144.9	10875
$f_{res,out}$	Hz	281.04	226.2	236

APPENDIX B: DIMENSIONS OF THE FABRICATED SCANNERS

Steel substrates have 300 μm thickness. Thinned regions are 150 μm thick. Mirror diameters are 3 mm for Design 1, Design 2, Design 3.2, and Design 3.3, 4 mm for Design 3.1, and 2.4 mm for Design 3.4.

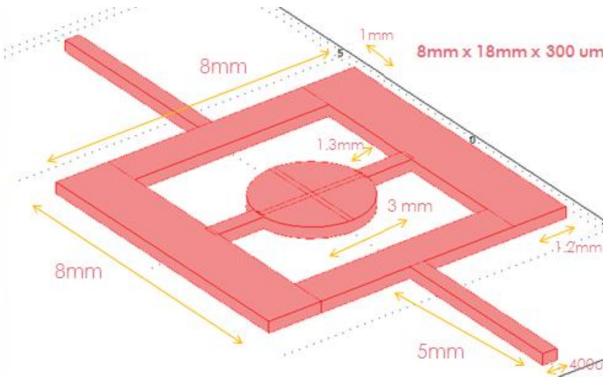

Figure B.1. Geometric dimensions of Design 1.

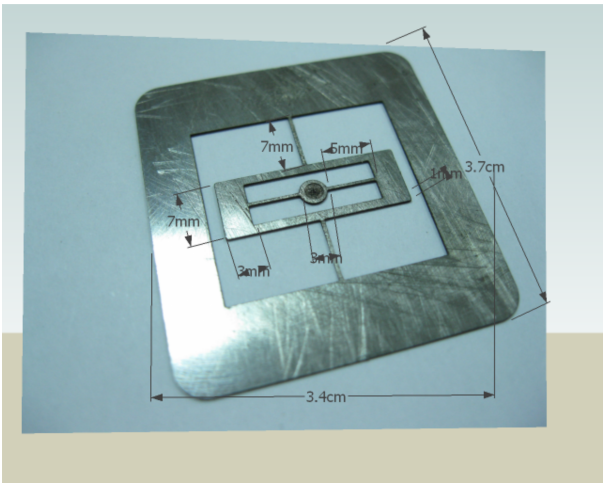

Figure B.2. Geometric dimensions of Design 2.

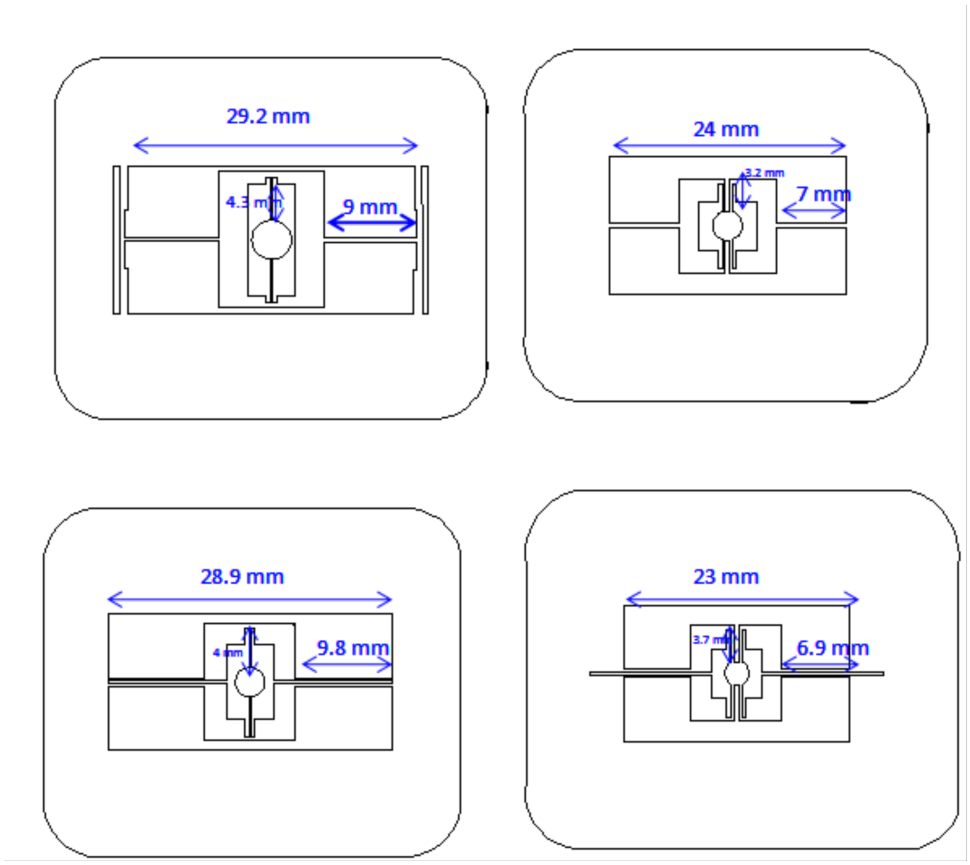

Figure B.3. Geometric dimensions of Designs 3.1, 3.2, 3.3, and 3.4.

APPENDIX C: SIMULATION RESULTS

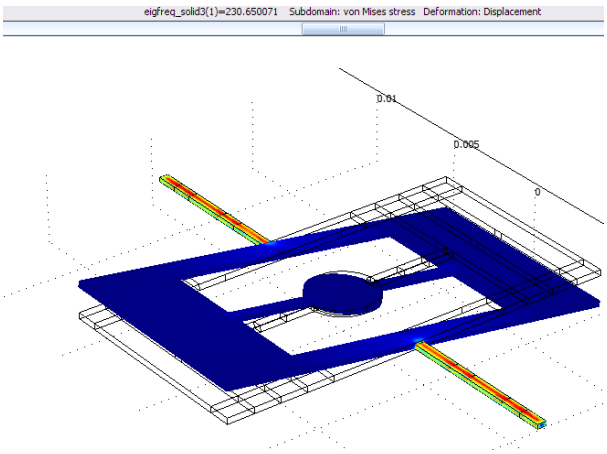

Figure C.1. Slow scan simulation of Design 1 at 230 Hz.

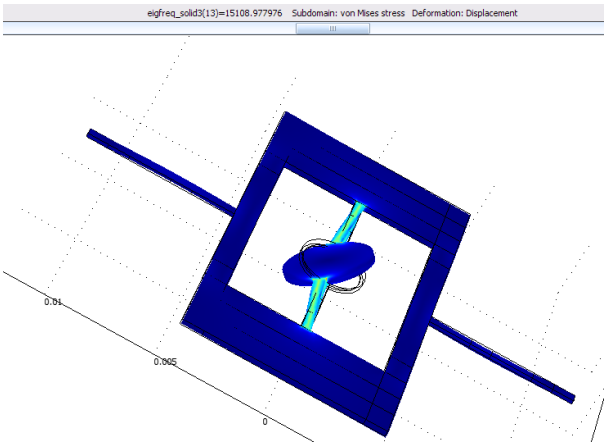

Figure C.2. Fast scan simulation of Design 1 at 15109 Hz.

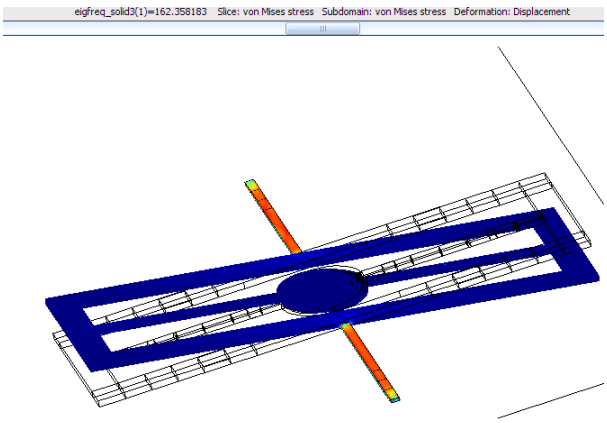

Figure C.3. Slow scan simulation of Design 2 at 162 Hz.

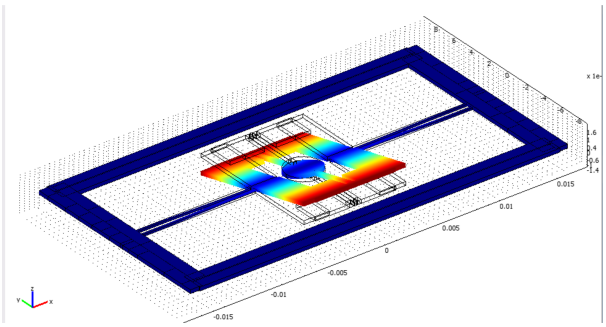

Figure C.4. Slow scan simulation of Design 3.2 at 221.5 Hz.

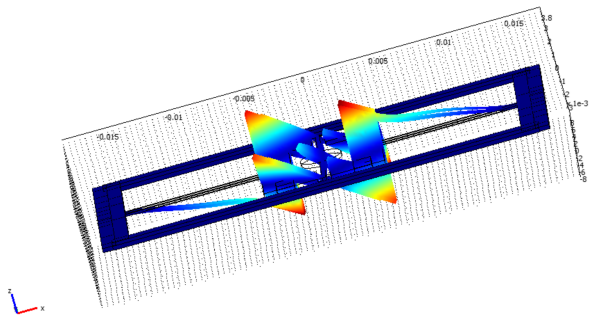

Figure C.5. Fast scan simulation of Design 3.2 at 6417 Hz.

REFERENCES

1. Urey H., D. W. and T. Osborn, "Optical Performance Requirements for MEMS-Scanner Based Microdisplays", *Conference on MOEMS and Miniaturized Systems, Proceedings of SPIE*, Vol. 4178, pp. 176–185, 2000.

2. Ephus, *ScanImage r3.6.x Documentation*, 2010, `http://www.neuroptikon.org/projects/display/ephus/`, online; accessed at September 2011.

3. Motamedi, M., *MOEMS: Micro-Opto-Electro-Mechanical Systems*, Press Monographs, SPIE Press, 2005.

4. Judy, J. and R. Muller, "Magnetically Actuated, Addressable Microstructures", *Journal of Microelectromechanical Systems*, Vol. 6, No. 3, pp. 249 –256, 1997.

5. Gokdel, Y. D., S. Mutlu and A. D. Yalcinkaya, "Self-Terminating Electrochemical Etching of Stainless Steel for the Fabrication of Micro-Mirrors", *Journal of Micromechanics and Microengineering*, Vol. 20, No. 9, p. 095009, 2010.

6. Beiser, L., *Laser Scanning Notebook*, SPIE Optical Engineering Press, Bellingham,WA, 1992.

7. Urey, H., "MEMS Scanners for Display and Imaging Applications", *Proceedings of SPIE*, Vol. 5604, pp. 218–229, 2004.

8. Hagelin, P. M., *Micromachined Mirrors for Raster-Scanning Displays and Optical Fiber Switches*, Ph.D. Thesis, University of California Davis, 2000.

9. Thomas, R., J. Guldberg, H. Nathanson and P. Malmberg, "The Mirror-Matrix Tube: A Novel Light Valve for Projection Displays", *IEEE Transactions on Electron Devices*, Vol. 22, No. 9, pp. 765–775, 1975.

10. Petersen, K. E., "Micromechanical Light Modulator Array Fabricated on Silicon",

Applied Physics Letters, Vol. 31, No. 8, pp. 521–523, 1977.

11. Petersen, K. E., "Silicon Torsional Scanning Mirror", *IBM Journal of Research and Development*, Vol. 24, No. 5, pp. 631–637, 1980.

12. Yalcinkaya, A., H. Urey, D. Brown, T. Montague and R. Sprague, "Two-Axis Electromagnetic Microscanner for High Resolution Displays", *Journal of Microelectromechanical Systems*, Vol. 15, No. 4, pp. 786–794, 2006.

13. Hooker R. B., B. C., *Scanned Light Beam Imaging Method and Apparatus*, US 4414583, 1983, "US Patent 4414583".

14. Hofmann, U., S. Muehlmann, M. Witt, K. Dorschel, R. Schutz and B. Wagner, "Electrostatically Driven Micromirrors for a Miniaturized Confocal Laser Scanning Microscope", *Proceedings of SPIE*, Vol. 3878, pp. 29–38, 1999.

15. Bifano, T. G., J. Perreault, R. Krishnamoorthy Mali and M. N. Horenstein, "Microelectromechanical Deformable Mirrors", *IEEE Journal of Selected Topics in Quantum Electronics*, Vol. 5, No. 1, pp. 83–89, 1999.

16. Lin, H.-Y. and W. Fang, "Rib-Reinforced Micromachined Beam and Its Applications", *Journal of Micromechanics and Microengineering*, Vol. 10, No. 1, p. 93, 2000.

17. Lee, D., U. Krishnamoorthy, K. Yu and O. Solgaard, "Single-Crystalline Silicon Micromirrors Actuated by Self-Aligned Vertical Electrostatic Combdrives with Piston-Motion and Rotation Capability", *Sensors and Actuators A: Physical*, Vol. 114, No. 2-3, pp. 423–428, 2004.

18. Kwon, S., V. Milanovic and L. Lee, "A high aspect ratio 2D gimbaled microscanner with large static rotation", *IEEE/LEOS International Conference on Optical MEMS, 2002. Conference Digest.*, pp. 149 – 150, 2002.

19. Zara, J. M. and S. W. Smith, "Optical Scanner Using a MEMS Actuator", *Sensors and Actuators A: Physical*, Vol. 102, No. 1-2, pp. 176–184, 2002.

20. Sasaki, M., T. Yamaguchi, J. Song, K. Hane, M. Hara and K. Hori, "Optical Scanner on a Three-Dimensional Microoptical Bench", *Journal of Lightwave Technology*, Vol. 21, No. 3, pp. 602–608, 2003.

21. Schweizer, S., S. Calmes, M. Laudon and P. Renaud, "Thermally Actuated Optical Microscanner with Large Angle and Low Consumption", *Sensors and Actuators A: Physical*, Vol. 76, No. 1-3, pp. 470–477, 1999.

22. Kobayashi, T., R. Maeda, T. Itoh and R. Sawada, "Smart Optical Microscanner with Piezoelectric Resonator, Sensor, and Tuner Using Pb(Zr,Ti)O3 Thin Film", *Applied Physics Letters*, Vol. 90, No. 18, pp. 183514–183517, 2007.

23. Lin, W.-M., A. Schroth, S. Matsumoto, C. Lee and R. Maeda, "Two-Dimensional Microscanner Actuated by PZT Thin Film", *Society of Photo-Optical Instrumentation Engineers (SPIE) Conference Series*, Vol. 3892, pp. 133–140, Oct. 1999.

24. Wagner, B. and W. Benecke, "Microfabricated Actuator with Moving Permanent Magnet", *Micro Electro Mechanical Systems, 1991*, pp. 27–32, MEMS '91, Proceedings. IEEE, 1991.

25. Bernstein, J., W. Taylor, J. Brazzle, C. Corcoran, G. Kirkos, J. Odhner, A. Pareek, M. Waelti and M. Zai, "Electromagnetically Actuated Mirror Arrays for Use in 3-D Optical Switching Applications", *Journal of Microelectromechanical Systems*, Vol. 13, No. 3, pp. 526–535, 2004.

26. Houlet, L., P. Helin, T. Bourouina, G. Reyne, E. Diffour-Gergam and H. Fujita, "Movable Vertical Mirror Arrays for Optical Microswitch Matrixes and Their Electromagnetic Actuation", *IEEE Journal of Selected Topics in Quantum Electronics*, Vol. 8, No. 1, pp. 58–63, 2002.

27. Wagner, B., M. Kreutzer and W. Benecke, "Linear and Rotational Magnetic Micromotors Fabricated Using Silicon Technology", *Micro Electro Mechanical Systems, 1992*, pp. 183–189, MEMS '92, Proceedings. IEEE, feb 1992.

28. Okano, Y. and Y. Hirabayashi, "Magnetically Actuated Micromirror and Measurement System for Motion Characteristics Using Specular Reflection", *IEEE Journal of Selected Topics in Quantum Electronics*, Vol. 8, No. 1, pp. 19–25, 2002.

29. Sadler, D., T. Liakapoulos and C. Ahn, "A Universal Electromagnetic Microactuator Using Magnetic Interconnection Concepts", *Journal of Microelectromechanical Systems*, Vol. 9, No. 4, pp. 460–468, 2000.

30. Lagorce, L. K., O. Brand and M. G. Allen, "Magnetic Microactuators Based on Polymer Magnets", *Journal Of Microelectromechanical Systems*, Vol. 8, No. 1, pp. 2–9, 1999.

31. Liu, C. and Y. Yi, "Micromachined Magnetic Actuators Using Electroplated Permalloy", *Magnetics, IEEE Transactions on*, Vol. 35, No. 3, pp. 1976 –1985, 1999.

32. Usta, B. K., Y. Gokdel and A. D. Yalcinkaya, "Selectively Thinned Stainless Steel Scanners Through Electrical Discharge Machining", *International Conference on Optical MEMS and Nanophotonics (OPT MEMS)*, aug. 2011.

33. Gokdel, Y. D., B. Sarioglu, S. Mutlu and A. D. Yalcinkaya, "Design and Fabrication of Two-Axis Micromachined Steel Scanners", *Journal of Micromechanics and Microengineering*, Vol. 19, No. 7, p. 075001, 2009.

34. AKSteel, *SS 420 Datasheet*, 2007, `http://www.aksteel.com/pdf/markets-products/stainless/martensitic/`, online; accessed at July 2011.

35. Iseki, T., M. Okumura and T. Sugawara, "Shrinking Design of a MEMS Optical Scanner Having Four Torsion Beams and Arms", *Sensors and Actuators A: Physical*, Vol. 164, No. 1-2, pp. 95–106, 2010.

36. Young, W. C. and R. G. Budynas, *Roark's Formulas for Stress and Strain*, 7th Edition, McGraw-Hill, 2002.

37. Urey, H., C. Kan and W. O. Davis, "Vibration Mode Frequency Formulae for Mi-

cromechanical Scanners", *Journal of Micromechanics and Microengineering*, Vol. 15, No. 9, pp. 1713–1721, 2005.

38. NASA Structural Engineering Division, N. A. and S. A. L. B. J. S. Center, *Process Specification for Electropolishing of Corrosion-Resistant Steel*, 2002, `/mmptdpublic.jsc.nasa.gov/prc/7227a.doc/`, online; accessed at August 2011.

39. Crichton, T., *Electropolishing 420 SS Stainless Steels*, 2009, `http://www.finishing.com/538/78.shtml`, online; accessed at August 2011.

40. Usta, M., *VGA Projection Display Using Electromagnetically Actuated Steel Micromirrors*, MS Thesis, Bogazici University, September 2011, (Submitted).